A state-dependent multilaminate constitutive model for anisotropic sands

Bayraktaroglu, Hilmi; Hicks, Michael A.; Korff, Mandy; Galavi, Vahid

DOI
10.1680/jgeot.22.00165

Publication date
2023

Document Version
Final published version

Published in
Geotechnique

Citation (APA)
Bayraktaroglu, H., Hicks, M. A., Korff, M., & Galavi, V. (2023). A state-dependent multilaminate constitutive model for anisotropic sands. *Geotechnique*, *74*(12), 1343-1359. https://doi.org/10.1680/jgeot.22.00165

A state-dependent multilaminate constitutive model for anisotropic sands

HILMI BAYRAKTAROGLU*, MICHAEL A. HICKS†, MANDY KORFF‡ and VAHID GALAVI§

Experimental studies show that initial fabric and its evolution under different stress paths greatly influences soil behaviour. Even though different sample preparation methods create different inherent anisotropies and cause different material responses, the same initial fabric structure under different stress paths also results in different material behaviours. In this paper, a simple state-dependent, bounding surface-based elastoplastic constitutive model, which can simulate the anisotropic nature of sands including the effect of principal stress rotation, is described. The model is developed based on a semi-micromechanical concept within the multilaminate framework and, to include the inherent anisotropy of sand, a deviatoric fabric tensor describing the initial microstructure is introduced. In addition, a fabric evolution rule compatible with anisotropic critical state theory is employed to describe the evolving fabric structure and induced anisotropy towards the critical state. In contrast to the classical strain-driven formulation for fabric evolution, a micro-level evolution rule is proposed. This paper presents concise theoretical aspects of the multilaminate framework and the anisotropic elastoplastic constitutive formulation. The model's capability under drained and undrained monotonic loading conditions at different stress states, relative densities and principal stress orientations is demonstrated by simulating experimental data for Toyoura sand.

KEYWORDS: anisotropy; constitutive relations; fabric/structure of soils; plasticity; sands

INTRODUCTION

The anisotropic nature of soil results in direction-dependent behaviour. Experimental studies carried out by varying stress paths and rotating principal stresses using simple and torsional shear tests show that soils with similar initial fabrics (i.e. undergoing the same sample preparation method and consolidated under the same confining pressure) may show drastic differences in response. In the case of sands, the response can range from highly contractive flow liquefaction to dilative behaviour (with no liquefaction) depending on the orientation of loading and fabric direction (Nakata *et al*., 1998; Uthayakumar & Vaid, 1998; Yoshimine *et al*., 1998; Sivathayalan & Vaid, 2002; Yang *et al*., 2008; Woo & Salgado, 2015). Similar fabric effects have also been observed in various types of boundary value problems. Azami *et al*. (2010) and Oda & Koishikawa (1979) studied the influence of fabric anisotropy on the bearing capacity and settlement of footings resting on layered sands. Qin *et al*. (2016) conducted centrifuge tests on saturated sands and observed the significant influence of deposition angle on excess pore pressure development.

One of the most common methods in the literature for handling the complex behaviour arising from the anisotropic nature of soil is to define a second-order fabric tensor approximating the soil microstructure. For this purpose, even though it is possible to formulate a tensorial quantity based on continuum level phenomenological observations, it is more reliable and physically consistent to statically describe the initial composition of the microstructure based on granular level observations such as the spatial orientation of particles, voids or contact networks. Following the initial description of the fabric (i.e. inherent anisotropy), an evolution rule can be formulated to incorporate the influence of the changing microstructure. In the literature, there are examples of models incorporating either an evolution rule (Wan & Guo, 2001; Li & Dafalias, 2012; Papadimitriou *et al*., 2019; Petalas *et al*., 2020; Yang *et al*., 2020; Zhao & Kruyt, 2020; Norouzi & Lashkari, 2021) or a fixed fabric tensor throughout the shearing process (Li & Dafalias, 2002, 2004; Dafalias *et al*., 2004; Yang *et al*., 2008; Yao *et al*., 2017). Although the models with a fixed fabric adequately simulate the soil behaviour, many recent granular level experimental and numerical observations carried out using X-ray computed tomography (CT) and the discrete-element method (DEM), respectively, show that anisotropic behaviour is not a fixed phenomenon arising solely from the initial depositional formation process, but an evolving phenomenon where a continuous evolution of the fabric composition takes place towards its critical state value (Li & Li, 2009; Fu & Dafalias, 2011; Kruyt, 2012; Guo & Zhao, 2013; Fu & Dafalias, 2015; Wang *et al*., 2017; Yang & Wu, 2017; Wiebicke, 2020; Wiebicke *et al*., 2020; Zhao & Kruyt, 2020; Zhao *et al*., 2021). Moreover, using a fixed fabric formulation may also lead to a deviation from a unique critical state line (CSL), which is considered to be independent of soil fabric.

In continuum models, fabric tensors are used to modify either the constitutive formulations or the input stresses. In order to modify the constitutive ingredients, a fabric

Manuscript received 16 May 2022; revised manuscript accepted 13 January 2023.
Discussion on this paper is welcomed by the editor.

* Section of Geo-Engineering, Faculty of Civil Engineering and Geosciences, Delft University of Technology, Delft, the Netherlands (Orcid:0000-0003-3878-4026).
† Section of Geo-Engineering, Faculty of Civil Engineering and Geosciences, Delft University of Technology, Delft, the Netherlands (Orcid:0000-0002-7603-7040).
‡ Section of Geo-Engineering, Faculty of Civil Engineering and Geosciences, Delft University of Technology, Delft, the Netherlands (Orcid:0000-0003-1922-9609).
§ DIANA FEA BV, Delft, the Netherlands; formerly Deltares, Department of Geo-Engineering, Delft, the Netherlands (Orcid:0000-0002-1281-8104).

anisotropy variable (FAV) was derived by Li & Dafalias (2012) as a function of the loading direction and fabric orientation, and a scalar measure of fabric is then incorporated into the relevant constitutive equations. In the case of stress modification, a modified stress tensor describing the strong force network is calculated (Wan & Guo, 2001; Yao *et al*., 2017). In contrast to the applied stress, the modified stress incorporates the effect of soil fabric and describes a modified isotropic scenario with a different stress state.

In the multilaminate framework, independently evolving constitutive ingredients at so-called sampling planes enable a model to simulate the effects of induced anisotropy and principal stress rotation intrinsically – that is without additional model parameters and mathematical complexity (Schweiger *et al*., 2009). However, the influence of initial soil fabric needs to be added and, in this regard, the existence of sampling planes, their spatial orientations and independently evolving deformation histories provide a unique and physically understandable way to formulate anisotropy.

The multilaminate framework was first proposed by Pande & Sharma (1983) for cohesive soils. Similar semi-micromechanical approaches, such as the microplane framework, were also developed (Prat & Bažant, 1991). Then, Galavi (2007) and Schweiger *et al*. (2009) introduced strength anisotropy in the multilaminate framework by incorporating the microstructure tensor proposed by Pietruszczak & Mroz (2000), in such a way that the ingredients of the Mohr–Coulomb failure criterion, namely friction angle and cohesion, were distributed over the sampling planes. However, even though these models provide reasonable performance and simulation capabilities, none of them is state dependent. Critical state-based, state-dependent multilaminate or similar semi-micromechanical models have been developed by Fang (2003), Chang & Sture (2006), Sadrnejad & Shakeri (2017) and Dashti *et al*. (2019). However, none of these models addressed or investigated fabric anisotropy and its evolution. The aim of this paper is to fill that gap with a simple, easy to understand anisotropic model compatible with the premises set out by anisotropic critical state theory (ACST) as proposed by Li & Dafalias (2012).

Note that, in this paper, the term 'micro' refers to within sampling planes where the inner structure and micro-level deformations are idealised. Second-order tensors and vector quantities are denoted by bold characters, the time derivative of a quantity is represented by a superposed dot, the juxtaposition of two vectors indicates their dot product, $||$ is used to denote the magnitude of a vector and the definitions of the tensorial operations are as follows:

$$\boldsymbol{A} : \boldsymbol{B} = A_{ij}B_{ij} \quad \boldsymbol{A} \cdot \boldsymbol{B} = A_{ik}B_{kj} \quad \mathrm{tr}(\boldsymbol{A}) = A_{ii}$$
$$\boldsymbol{A}^* = \boldsymbol{A} - \mathrm{tr}(\boldsymbol{A}) \cdot \boldsymbol{I}/3 \quad \|\boldsymbol{A}\| = \sqrt{\boldsymbol{A} : \boldsymbol{A}}$$

MULTILAMINATE FRAMEWORK

In classical continuum mechanics, the components of the stress and strain tensors are defined on an infinitesimal cubic element. The invariants obtained from these tensors are either directly used in triaxial stress space, or generalised to three-dimensional (3D) stress space using Lode angle-dependent interpolating functions, to formulate constitutive models. In both cases, the investigation of the directional dependency of the material requires a second-order fabric tensor.

From the theoretical point of view, a stress state defined by a spherical element can be used to take account of the contribution of an infinite number of planes/directions, with relevant integration being carried out over its surface, but this is practically impossible. The multilaminate framework proposes an alternative for approximating the ideal case, by employing a convex polyhedron approximating a unit sphere and utilising a numerical integration scheme, as illustrated in Fig. 1. The numerical integration is a closed-form solution, carried out using a finite number of planes with their predefined orientations (which are called sampling or integration planes) and weight coefficients. This straightforward integration process also provides flexibility for using a wide range of sampling planes. The accuracy and computational performance of various sampling plane configurations can be found in Ehret *et al*. (2010). In this paper, an orthogonally symmetric polyhedron with 66 sampling planes has been employed. However, owing to the symmetry, integration has been carried out over the half space using only 33 sampling planes. A complete discussion of the multilaminate framework is beyond the scope of this paper, as the mathematics of the polyhedron, the advantages of orthogonal symmetry and the calculation of weight coefficients and

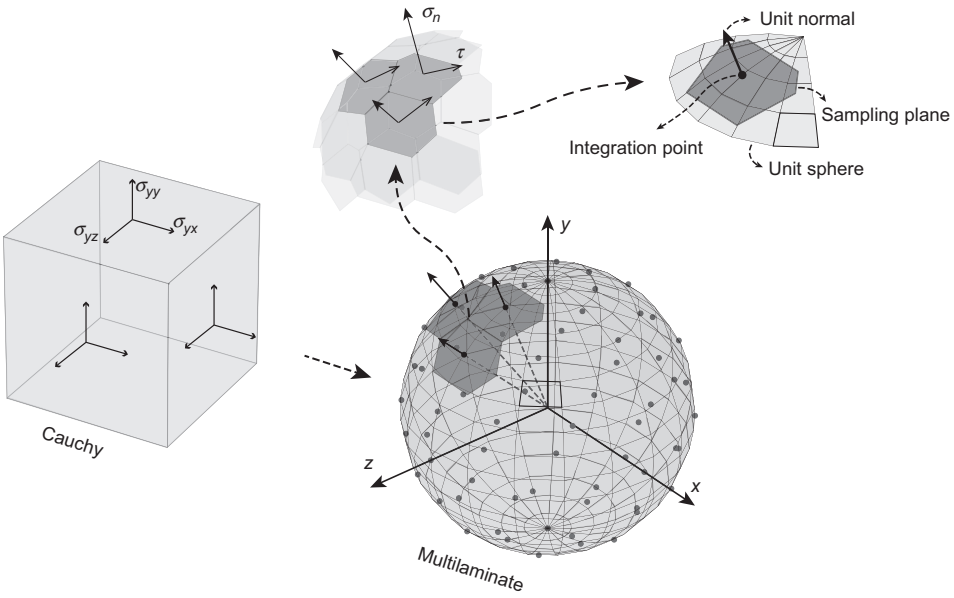

Fig. 1. Macro–micro-level stress transformation and local stress components

numerical integration can be found in Fliege & Maier (1996), Bažant & Oh (1986), Ehret *et al*. (2010) and Stroud (1971). In Fig. 1, a polyhedron approximating a unit sphere is obtained by placing 2×33 sampling planes an equal distance from an integration point.

Workflow in multilaminate framework

In the multilaminate framework, the global deformation is assumed to result from the micro-level internal sliding taking place at each sampling plane. The resistance against shearing and the resultant volumetric changes are calculated individually at each of these planes and then integrated numerically over the unit sphere to obtain their global counterparts. In this section, this link between macro- and micro-level behaviours will be described.

Unlike the classical constitutive modelling approach, where there is a direct link between the stress and strain tensors, in the multilaminate framework constitutive models are defined at sampling planes using local stress and strain vectors. At an integration point, the transformation of a Cauchy stress tensor $\boldsymbol{\sigma}'$ into micro-level normal and shear stresses for an arbitrary plane i can be defined as follows

$$\begin{aligned}\boldsymbol{\sigma}_i' &= (\mathbf{T}_i)^{\mathrm{T}}\boldsymbol{\sigma}' = \begin{pmatrix}\sigma_n' \\ \tau\end{pmatrix} = \begin{pmatrix}\sigma_{p,n}' + \sigma_{\mathrm{dev},n}' \\ \tau\end{pmatrix} \\ &= \begin{pmatrix} p' + (\boldsymbol{\sigma}^* \boldsymbol{n}_i)\boldsymbol{n}_i \\ \left|\boldsymbol{\sigma}^* \boldsymbol{n}_i - ((\boldsymbol{\sigma}^* \boldsymbol{n}_i)\boldsymbol{n}_i)\boldsymbol{n}_i\right| \end{pmatrix}\end{aligned} \tag{1}$$

where the subscript i denotes the ith plane; $\boldsymbol{\sigma}_i'$ is the resultant traction stress vector with local components σ_n' and τ; $\boldsymbol{\sigma}^*$ is the deviatoric part of $\boldsymbol{\sigma}'$; $\sigma_{\mathrm{dev},n}'$ is the magnitude of the deviatoric stress component in the direction normal to the plane and is equal to $(\boldsymbol{\sigma}^* \boldsymbol{n}_i)\boldsymbol{n}_i$; $\sigma_{p,n}'$ is the mean effective stress and is equal to p' at each plane; $\boldsymbol{n}_i$ is the unit normal (or direction cosine) vector; and $\mathbf{T}_i$ is the transformation matrix, which contains partial derivatives of the local effective stress vector with respect to the global effective stress vector. The detailed derivation of the transformation matrix $\mathbf{T}_i$ can be found in Galavi (2007). The stress transformation concept formulated in equation (1) is schematically shown in Fig. 1.

A consistent micromechanical system should satisfy both static and kinematic constraints. In this framework, projecting the global stress tensor onto the sampling planes ensures the static constraint. In order to fulfil the kinematic constraint, instead of the normal–tangential (NT) split, the volumetric–deviatoric (VD) split method has been used such that the micro-level normal stress components are assumed to be the projection of the mean and deviator stress tensors, equation (1). Further details regarding thermodynamical consistency of the framework can be found in Bažant & Caner (2005).

It is important to note that the sampling plane orientations are defined independently of the statistical distribution of the contact force vectors – that is, fabric – to create a unit sphere that does not evolve during deformation. This can be shown using the fabric definition provided by Satake (1978)

$$\phi_{kj} = \frac{1}{N_{\mathrm{c}}} \sum_{i=1}^{N_{\mathrm{c}}} n_k^i n_j^i \tag{2}$$

where ϕ_{kj} is the statistical distribution of the contact normals; N_{c} is the number of contacts (in this model the contact force network is assumed to be idealised by sampling planes, so that $N_{\mathrm{c}} = 33$); n_k^i is the component of the unit contact normal in direction k for the ith contact (in this model the orientations of the idealised contacts/sampling planes are defined using their unit normals). In this model, equation (2) yields a second-order identity tensor $\boldsymbol{I}$ and any deviation from $\boldsymbol{I}$ denotes an anisotropic contact force network, which can be captured by modifying the shape of the unit sphere illustrated in Fig. 1 through the use of a second-order fabric tensor modifying the unit normal vectors. However, in this paper, stress modification has been omitted. An evolving fabric tensor will be used only for the modification of the constitutive ingredients.

Following the calculation of the local stress increments, local constitutive models are employed to calculate the corresponding micro-level plastic strain increments

$$\mathrm{d}\boldsymbol{\varepsilon}_i^{\mathrm{p}} = \mathrm{d}\lambda_i \frac{\partial g_i}{\partial \boldsymbol{\sigma}_i'} \tag{3}$$

where $\mathrm{d}\lambda_i$ and g_i are the plastic multiplier and plastic potential function of the ith plane. Finally, the plastic contribution of each sampling plane is transferred back to the macro level using numerical integration by means of the principle of complementary virtual work over the unit surface area S

$$\mathrm{d}\boldsymbol{\varepsilon}^{\mathrm{p}} = \int_S \mathbf{T}_i \mathrm{d}\boldsymbol{\varepsilon}_i^{\mathrm{p}} \mathrm{d}S \cong 3 \cdot \sum_{i=1}^{n_{\mathrm{sp}}} \mathbf{T}_i \mathrm{d}\boldsymbol{\varepsilon}_i^{\mathrm{p}} w_i \tag{4}$$

where $\mathrm{d}\boldsymbol{\varepsilon}^{\mathrm{p}}$ is resultant global plastic strain increment; $n_{\mathrm{sp}} = 33$ is the number of sampling planes; and w_i is the weight coefficient of the ith plane such that $\sum_1^{n_{\mathrm{sp}}} w_i = 1{\cdot}0$. A detailed derivation of equation (4) can be found in Carol & Bazant (1997).

The global plastic strain increments are calculated in a loop which continues until all the micro-level stresses are returned back to admissible stress states. It should be emphasised that the evolution of the local plastic strains depends on the loading history on the corresponding plane. While some planes undergo elastic deformations, others may show a plastic response. Eventually, close to failure, plasticity concentrates on one or a few planes (Sánchez *et al*., 2008; Galavi & Schweiger, 2010). Fig. 2 shows the polar distribution of the micro stress invariants, σ_n' and τ, and their varying magnitudes for a given global stress state in Voigt form $\sigma = [100 \quad 100 \quad 300 \quad 0 \quad 0 \quad 100]^{\mathrm{T}}$. In this figure, the different magnitudes of local normal stresses (represented by σ_n' in Fig. 2) result in varying material states in each direction and the varying local shear stresses (represented by τ in Fig. 2) yield different plastic strain accumulations in each direction.

It is important to note that, during the course of deformation at each sampling plane, a varying magnitude of micro-level plastic strains triggers a unique hardening evolution (independent from each other). At the critical state, the coupling between sliding and volumetric behaviour diminishes, and an equilibrium state is reached in which the applied global stress is balanced by the local normal and shear components.

Some of the potential advantages of using the multilaminate framework are given below.

(*a*) Any deviation from the hydrostatic axis leads to varying normal stresses over the sampling planes, which results in anisotropic state variables, which control the hardening and volumetric behaviours in different directions.
(*b*) Storing state variables independently at each sampling plane provides for a history-dependent anisotropic mobilisation process without mathematical complexity.
(*c*) Lode angle dependency is implicitly obtained through the variation of micro-level stress ratios at the critical state.

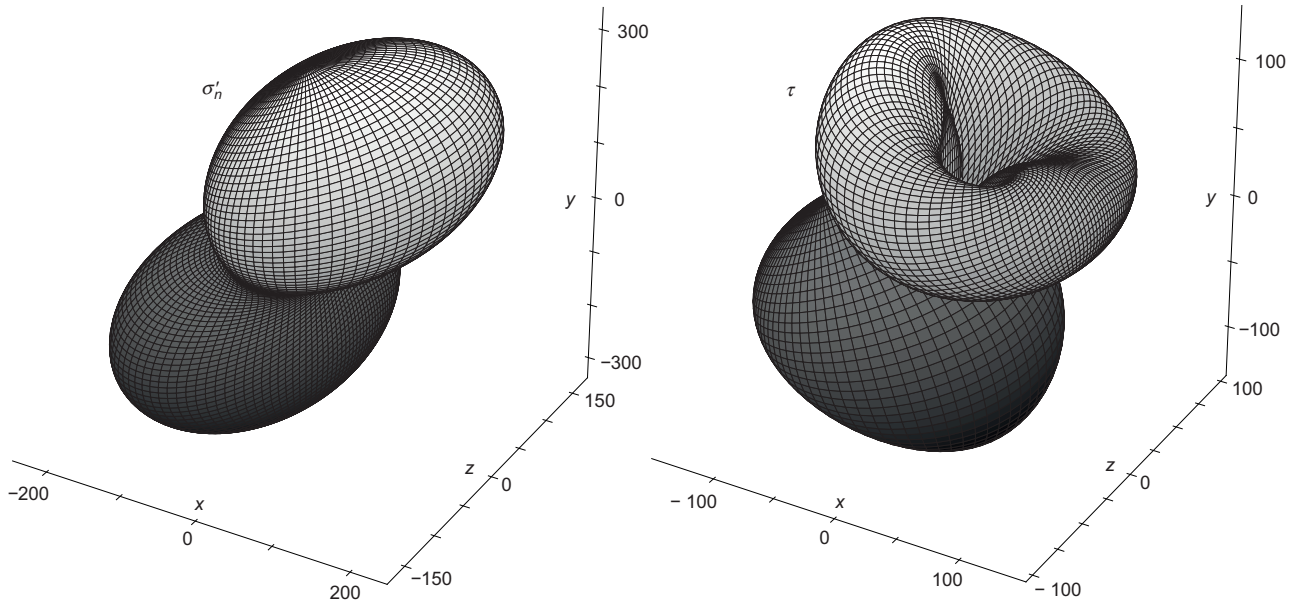

Fig. 2. Polar distribution of micro-level stress invariants for a given stress state in Cartesian coordinate system

(*d*) There are no singular points which generally require special treatments for the convergence.
(*e*) The independent mobilisation processes in different sampling planes enables the framework to be parallelised.

There is a common misconception that, for the multilaminate framework employing a specific constitutive model at the sampling planes, the speed of the solution will be slower than that for the same constitutive model's generalised stress space implementation by a factor equal to the number of sampling planes. It should be noted that, during a simulation, most of the computational effort is spent during the plasticity phase, where some iterative procedures are needed in order to achieve convergence. In the multilaminate framework, plastic deformations are not observed on all sampling planes simultaneously; only a limited number of sampling planes show a plastic response, while the rest are in the elastic range.

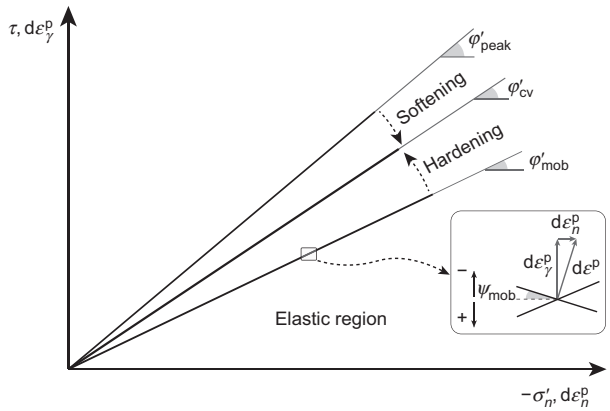

Fig. 3. Evolution of yield function, failure line and representation of the non-associative flow rule

MICRO-LEVEL CONSTITUTIVE FORMULATION

In this section, a simple state-dependent, elastoplastic, anisotropic constitutive model is presented. The anisotropy formulation of the model is based on the ACST proposed by Li & Dafalias (2012), in which, together with the critical state requirements, an additional critical measure of the fabric anisotropy is defined.

All mathematical equations given in this section are for a representative sampling plane. The sign convention is that tensile stresses and strains are positive.

Yield function and critical state formulation

The well-known Coulomb criterion has been utilised as the yield criterion through use of the mobilised angle of internal friction, φ'_{mob} – that is

$$f = \tau + \sigma'_n \tan \varphi'_{\mathrm{mob}} = 0 \tag{5}$$

Stress states inside the yield surface are associated with elastic behaviour, and the limiting yield surface represents the failure surface, outside which stress states are not admissible, Fig. 3. The use of equation (5) in a multilaminate framework consisting of 33 sampling planes yields a Mohr–Coulomb type yield surface in global stress space. Note that the exact shape of this global yield surface depends greatly on the number of sampling planes employed. Increasing the number of sampling planes moves the resultant global yield surface closer to the Mohr–Coulomb yield surface. A comparison showing various yield surfaces in the normalised deviatoric plane, including the one originally proposed by Argyris *et al.* (1974) and later employed by the Sanisand family of models, Matsuoka–Nakai, Mohr–Coulomb and multilaminate, is given in Fig. 4. Note that, for the yield surface implied by Multilaminate, each data point represents the result of an actual simulation.

The intermediate locations of the yield surface are defined by the hardening/softening formulation. This formulation is based on the state-dependent hyperbolic hardening formulation originally proposed by Wan & Guo (1998) and has been converted to its two-dimensional counterpart as follows

$$\tan \varphi'_{\mathrm{mob}} = \tan \varphi'_i + (\tan \varphi'_{\mathrm{cv}} - \tan \varphi'_i) \frac{\varepsilon^{\mathrm{p}}_{\gamma}}{A + \varepsilon^{\mathrm{p}}_{\gamma}} \cdot f_{\mathrm{d}} \tag{6}$$

in which the plastic shear strain $\varepsilon^{\mathrm{p}}_{\gamma}$ triggers the mobilisation of friction angle; φ'_i defines the size of the initial (innermost) elastic zone from which the mobilisation starts; φ'_{cv} stands for constant volume friction angle; and the plastic stiffness

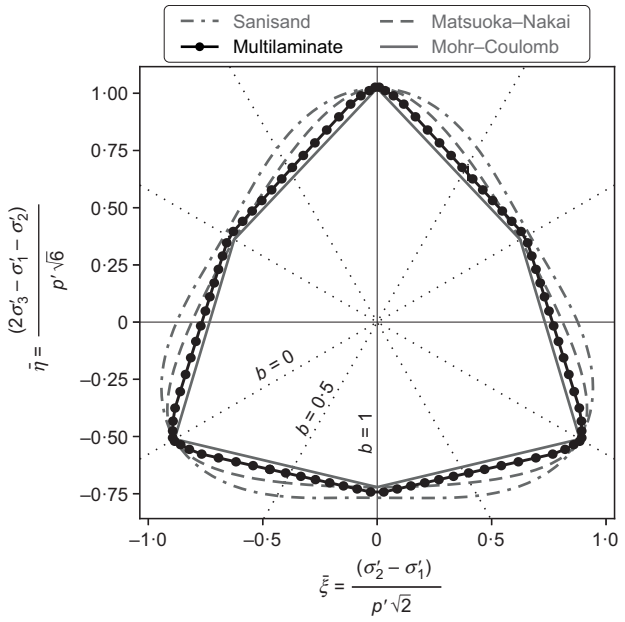

Fig. 4. Comparison of Sanisand with $M_c/M_c = 0{\cdot}75$, Matsuoka–Nakai, Mohr–Coulomb and multilaminate (with 33 planes) yield surfaces in the normalised deviatoric plane for $\varphi' = 31{\cdot}2^\circ$

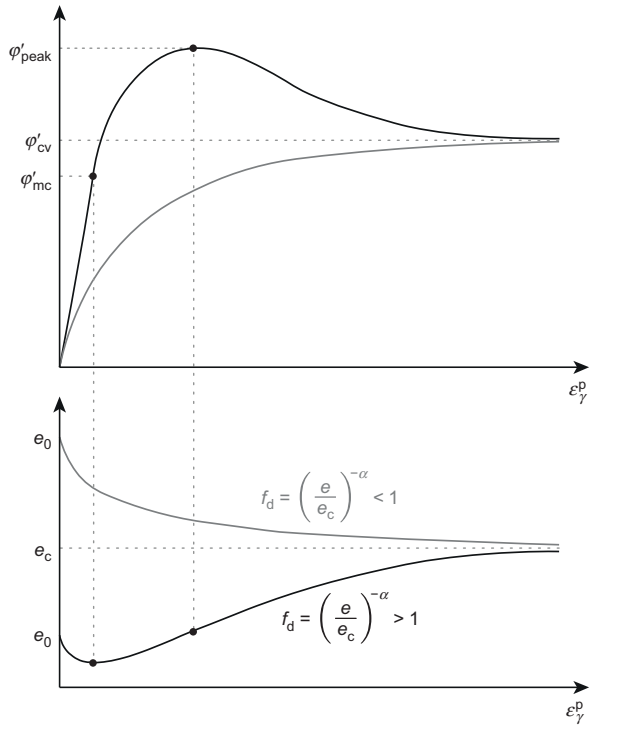

Fig. 5. Material responses modelled by the hardening/softening rule at sampling planes (Wan & Guo, 1998)

parameter A controls the speed of mobilisation such that, for a target mobilised friction angle, a larger A requires more plastic shear strain accumulation. The key ingredient f_d provides the state dependency, including the effects of both current stress and void ratio, and is given by Wan & Guo (1998)

$$f_d = \left(1 + \psi e_c^{-1}\right)^{-\alpha} = \left(\frac{e}{e_c}\right)^{-\alpha} \text{ with } e_c = e_{c,0} \exp\left[-\left(\frac{-\sigma_n'}{h_s}\right)^n\right] \tag{7}$$

where the critical void ratio at zero stress $e_{c,0}$ and model parameters h_s and n are used to define the location of the CSL in void ratio–effective stress space; $\psi = e - e_c$ is the state parameter (Been & Jefferies, 1985); and the exponential parameter α controls the peak friction angle. The idea of state dependency of the peak friction angle was first formulated by Wood *et al.* (1994) with a linear dependency on ψ and later translated into bounding surface plasticity by Manzari & Dafalias (1997). This linear dependency was replaced by an exponential function by Li & Dafalias (2000). However, in this paper the formulation proposed by Wan & Guo (1998) has been used. Upon reaching the critical state $e \to e_c$ and f_d unconditionally becomes equal to 1. It should be emphasised that, unlike a unique CSL, there is no specific predefined failure line. The failure surface (which can be considered as the integration of failure lines over the unit sphere) is formulated as a function of the critical and current void ratios. The schematic description of the hardening/softening by use of f_d is described in Fig. 5. Here, the term 'softening' does not refer to material instability encountered upon strain localisation, but is instead used to represent the material weakening following peak state.

Hyperbolic hardening formulations originating from the work of Duncan & Chang (1970) are commonly used in many constitutive models (Pietruszczak & Niu, 1992; Cubrinovski & Ishihara, 1998; Schanz *et al.*, 1999; Wan & Guo, 2004; Schweiger *et al.*, 2009; Galavi, 2021). However, this simple, yet effective formulation provides limited flexibility for highly non-linear soil behaviour. Experimental studies by Tatsuoka *et al.* (1993) and Cubrinovski & Ishihara (1998) showed that a constant A is not suitable for describing the variation in plastic shear modulus over a wide strain range and they proposed alternative formulations. Based on these observations, an alternative simpler form has been proposed by Galavi (2021), in which the value of A starts from $A_{mat,i}$ at small strain and exponentially increases to A_{mat} at large strain. In this paper, this formulation is further enhanced to include the effect of stress state and soil fabric by the addition of the last bracketed term as follows

$$A = \left\{\left[1 - \exp\left(\frac{-D_R}{A_{mat}}\varepsilon_\gamma^p\right)\right]A_{mat} + \exp\left(\frac{-D_R}{A_{mat}}\varepsilon_\gamma^p\right)A_{mat,i}\right\} \times \left[\left(\frac{-\sigma_n'}{p_{at}}\right)^{(n-1)} \exp\left(-k_{ani}A_{fab}^i\right)\right] \tag{8}$$

with

$$A_{mat,i} = \left(1 - \frac{D_R}{2}\right)\left(\frac{1}{G_{ratio}}\right)A_{mat} \tag{9}$$

Even though the original formulation proposed by Galavi (2021) captures the evolution of the plastic modulus, the omission of stress state dependency makes the calibration of A difficult over wide stress ranges. Moreover, from the anisotropy point of view, the inclusion of fabric in determining the plastic modulus is essential to capture different responses under different stress paths and/or fabric compositions at ultimate states. In equation (8), the addition of the exponential fabric term includes the fabric dependence of A over widely different loading directions. In this paper, k_{ani} is set equal to 1·0 and the loading path-dependent formulation of A_{fab}^i is given in equation (26).

It should be noted that the hardening formulation proposed by Wan & Guo (1998) has a number of drawbacks, as explained below.

(*a*) The hyperbolic type hardening formulation given in equation (6) requires an infinite plastic shear strain to

reach the critical state. In order to eliminate this problem, the value of constant A in the original formulation should be small enough to match the critical state relatively closely (i.e. $\varphi'_{mob} \rightarrow 0.999\varphi'_{cv}$) in a finite shear strain range. However, such a small value of A results in a very stiff behaviour, which generally does not match with experimental data. The proposed formulation in equation (8) enables the model to get relatively close to the critical state within a reasonable shear strain range, while at the same time matching experimental results.

(*b*) The use of plastic strain (which is not an experimentally measurable quantity) in the hardening formulation complicates the calibration procedure when the specimen is presheared. In such a scenario, for a given state, following the calculation of the friction angle from the test/data, the accumulated plastic strains can be back-calculated from equation (6).

From the critical state point of view, at the ultimate state the model yields the following conditions

$$\varepsilon_\gamma^p \rightarrow \infty,\ e \rightarrow e_c,\ f_d \rightarrow 1,\ \varphi'_{mob} \rightarrow \varphi'_{cv} \text{ and } \dot{f} \rightarrow 0$$

It should be emphasised that, in this framework, reaching the critical state does not necessarily mean that the mobilised friction angle at each plane $\varphi'_{mob,i}$ has reached the constant volume friction angle φ'_{cv}. Only planes with continuous plastic deformations yield $\varphi'_{mob,i} \rightarrow \varphi'_{cv}$ at the critical state and, as a result, the model globally yields a Lode angle-dependent φ'_{cs} (implicitly).

Finally, as shown in Fig. 3, no kinematic hardening formulation is included to capture the plasticity upon unloading. Even though some plasticity could be captured upon changing loading direction as a result of the activation of some new (i.e. previously not activated) planes, upon a complete loading reversal no additional sampling planes experience plasticity. As a result, upon a complete loading reversal, the stress state at each sampling plane falls into the elastic zone, which results in a global elastic response. The aim of future work is to improve the proposed model with a proper kinematic hardening formulation for modelling complex loading conditions such as stress principal axes rotation (SPAR) and cyclic loading conditions.

Flow rule

The evolution of plastic strains and return mapping are formulated using a non-associated flow rule in which the gradient of the plastic strain increment is controlled by the mobilised dilatancy angle, ψ_{mob}. Hence

$$g = \tau + \sigma'_n \tan \psi_{mob} = 0 \tag{10}$$

The coupling between the shearing and compaction/dilation mechanism is provided using a simple dilatancy formulation

$$-\frac{d\varepsilon_N^p}{d\varepsilon_\gamma^p} = \sin \psi_{mob} = \frac{\sin \varphi'_{mob} - \sin \varphi'_f}{1 - \sin \varphi'_{mob} \times \sin \varphi'_f} \tag{11}$$

The structure of equation (11) is identical to Rowe's (1962) stress dilatancy expression formulated in terms of mobilised friction and dilatancy angles by Vermeer & De Borst (1984). However, φ'_{cs} in the original formulation, which only refers to the ultimate condition, has been replaced by the state-dependent characteristic friction angle φ'_f. The state dependency of the phase transformation was first formulated as a linear function of the state parameter ψ by Manzari & Dafalias (1997) and later as a power function of the ratio e/e_c, as in equation (13), by Wan & Guo (1998). In this paper, the micromechanical derivation of φ'_f has been adopted from Wan & Guo (2014) as follows

$$\sin \varphi'_f = f_e \sin \varphi'_{cv} \tag{12}$$

and

$$f_e = \left(1 + \psi e_c^{-1}\right)^\beta = \left(\frac{e}{e_c}\right)^\beta \tag{13}$$

where the exponential parameter β is a model constant.

In the proposed formulation, the influence of void ratio and stress state on the dilatancy is introduced through the f_e formulation. It should be emphasised that towards the critical state, f_e evolves to 1 and equation (11) reduces to Rowe's dilatancy formulation.

As shown in Fig. 5, based on this formulation, at the phase transformation (or maximum contraction) point, by enforcing zero dilatancy the friction angle can be obtained from

$$\varphi'_{mc} = \sin^{-1}(f_e \sin \varphi'_{cv}) \tag{14}$$

For the elastoplastic formulation, at the beginning of shearing (i.e. at low mobilised friction angles) Rowe's dilatancy formulation together with equation (6) yields excessive plastic strains, which results in highly contractive behaviour and excessive pore pressure accumulation under undrained shearing. Hence, various modifications to Rowe's dilatancy formulation have been proposed (Schanz, 1998; Søreide, 2003; Wehnert, 2006), although none of these modifications provides a state-dependent solution for the aforementioned problem. A detailed comparison of the modifications can be found in Benz (2007) and Tsegaye *et al*. (2013). A similar excessive pore pressure accumulation in the vicinity of the hydrostatic axis is also observed in hypoplasticity, as pointed out in Niemunis (2003).

In this paper, in order to improve the undrained performance of the model in the small-strain range, plastic volumetric strains in the small-strain range are factored by k_{stiff}

$$k_{stiff} = \left(\frac{\gamma}{\gamma_{small}}\right)^{k_{el}} \leq 1{\cdot}0 \tag{15}$$

where the exponential parameter k_{el} controls the evolving small-strain effect. In this model, a linear link between k_{stiff} and the shear strain is assumed by setting $k_{el} = 1$. By employing equation (15), a mobilisation process that increases the size of the inner, most elastic zone without the build-up of excess pore pressure is obtained.

In this model, parameters f_d and f_e, as defined by equations (7) and (13), respectively, are used to obtain the state dependency. Alternatives to these formulations can be found in Li & Dafalias (2000) and Dafalias & Manzari (2004) as follows

$$f_d = \exp[-\alpha'(e - e_c)] \text{ and } f_e = \exp[\beta'(e - e_c)] \tag{16}$$

However, even though equations (7), (13) and (16) provide comparable results, and the parameters α and β have similar functionalities as α' and β', they are quantitatively different.

Elasticity formulation

The elasticity formulation is divided into two parts: small and large strain ranges. For large strains, an isotropic, state-dependent hypoelastic formulation proposed by Oztoprak & Bolton (2013) has been used. The influence of current effective stress on the elastic stiffness is controlled by the exponential parameter m. The relationship between m and stiffness parameter n, which is used together with the model

parameter h_s to define the CSL in e–p' space, was developed by Herle & Gudehus (1999) and Wegener & Herle (2012) such that $m = 1 - n$. As a result, beyond providing a comparable performance with the hypoelastic formulation proposed by Richart *et al*. (1970), equation (17) provides further flexibility through the exponential parameter m.

$$G = \frac{G_{\text{ref}} p_{\text{at}}}{(1+e)^3} \left(\frac{p'}{p_{\text{at}}} \right)^m \tag{17}$$

A question may arise concerning the necessity of employing a fabric-dependent anisotropic elasticity formulation. However, for the sake of simplicity an isotropic elasticity formulation has been employed in this model similar to many other ACST-based models (Dafalias *et al*., 2004; Papadimitriou *et al*., 2019; Petalas *et al*., 2020).

For the small-strain part of the model, a hyperbolic-type non-linear shear strain-dependent formulation from Santos & Correia (2001) has been employed

$$G_{\text{small}} = \frac{G_0}{1 + 0{\cdot}385(\gamma/\gamma_{0{\cdot}7})} \tag{18}$$

where G_0 refers to the maximum (elastic) shear modulus, and $\gamma_{0{\cdot}7}$ refers to the shear strain value at which the secant shear modulus reduces to 70% of its maximum value. For simplicity, the maximum shear modulus is calculated by factoring equation (17) with a model constant G_{ratio} – that is

$$G_0 = G_{\text{ratio}} G \tag{19}$$

Finally, the actual shear modulus used in the constitutive formulation is obtained as

$$G_{\text{act}} = \max(G_{\text{small}}, G) \tag{20}$$

Rearranging equations (17) and (18), a threshold small-strain value is defined as

$$\gamma_{\text{small}} = \frac{(G_{\text{ratio}} - 1)\gamma_{0{\cdot}7}}{0{\cdot}385} \tag{21}$$

for which $\gamma \leq \gamma_{\text{small}}$ falls into the small-strain range and otherwise the large-strain range. In this paper, small-strain elasticity is used to increase the accuracy of the model together with equation (15), rather than only amplifying the shear modulus upon loading reversal.

The above elasticity formulation is used to construct stiffness matrices for both the global system and the sampling planes. Even though the split method does not change the global stiffness matrix, local stiffness ingredients are calculated based on the split method used

$$\begin{bmatrix} \mathrm{d}\sigma_{p,n} \\ \mathrm{d}\sigma_{\text{dev},n} \\ \mathrm{d}\tau \end{bmatrix} = \begin{bmatrix} \dfrac{E}{1-2\nu'} & 0 & 0 \\ 0 & \dfrac{E}{1+\nu'} & 0 \\ 0 & 0 & \dfrac{E}{1+\nu'} \end{bmatrix} \begin{bmatrix} \mathrm{d}\varepsilon_v \\ \mathrm{d}\varepsilon_{q,n} \\ \mathrm{d}\gamma \end{bmatrix} \tag{22}$$

FABRIC ANISOTROPY AND ITS EVOLUTION

In this model, a modification of a recent framework called ACST proposed by Li & Dafalias (2012) has been adopted to handle the complex anisotropic soil behaviour. In ACST, control over dilative and contractive behaviours is established using a so-called dilatancy state line (DSL), which is obtained by modifying the CSL anisotropically for varying stress paths and fabric orientations. Even though there is no absolute consensus on the uniqueness of the CSL, recent experimental studies (Verdugo & Ishihara, 1996; Yoshimine & Kataoka, 2008; Salvatore *et al*., 2017) and many granular level numerical studies have shown that soil reaches a unique CSL independent of the stress path and fabric structure. In the ACST proposed by Li & Dafalias (2012), in order to satisfy the uniqueness of the CSL, the DSL is formulated in such a way that, independent from the initial fabric structure, it evolves towards the CSL and finally becomes identical to the CSL. In this paper, the theory of ACST has been adapted for use in the multilaminate framework where the constitutive formulations are defined at sampling planes.

The isotropic measure of the state of the soil given in equation (7) has been modified to derive the fabric-dependent DSL in void ratio–effective stress space introduced by Li & Dafalias (2012)

$$e_{\text{d}} = e_{\text{c}} + e_A \left(A^i_{\text{fab}} - 1 \right) \tag{23}$$

In equation (23), similar to most of the ACST-based models, the FAV A^i_{fab} evolves such that $A^i_{\text{fab}} \to 1$ towards the critical state, although its definition, which is given in equation (26), slightly differs from A_{fab} proposed by Li & Dafalias (2012). Following the introduction of the ACST, for model formulations involving the critical state parameter, $\psi = e - e_{\text{c}}$ is replaced by the dilatancy state parameter $\zeta = e - e_{\text{d}}$. In this model, the same thing is achieved by replacing the critical void ratio e_{c} in the f_{d} and f_{e} formulations (equations (7) and (13)) with the dilatancy void ratio, e_{d}. Note that the fabric parameter e_A is used to scale the downward movement of the DSL with respect to the CSL in e–p' space (Petalas *et al*., 2020).

Fabric tensor and vector

In this model, a contact normal-based cross-anisotropic fabric formulation has been employed. The deviatoric part of the initial microstructure tensor is described as

$$\boldsymbol{F}_{\text{in}} = \begin{bmatrix} F_{\text{h}} & 0 & 0 \\ 0 & F_{\text{v}} & 0 \\ 0 & 0 & F_{\text{h}} \end{bmatrix} \tag{24}$$

Here, the major principal fabric direction has been selected in the y-direction – that is the bedding plane is normal to the y-axis and cross-anisotropic idealisation yields the other two principal components to be equal. Since the above initial fabric tensor represents the normalised deviatoric part of the statistical distribution of the contact normal given in equation (2), $\boldsymbol{F}_{\text{in}}$ has to be traceless – that is $F_{\text{v}} = -2F_{\text{h}}$. Reorganising the above expression, a cross-anisotropic fabric tensor can be defined as

$$\begin{aligned} \boldsymbol{F}_{\text{in}} &= \frac{\boldsymbol{\phi}^*}{\|\boldsymbol{F}_{\text{c}}\|} = F_{\text{norm}} \cdot \boldsymbol{n}_{\text{F}} \\ &= \sqrt{\frac{3}{2}} |F_{\text{v}}| \begin{bmatrix} \dfrac{-1}{\sqrt{6}} & 0 & 0 \\ 0 & \dfrac{2}{\sqrt{6}} & 0 \\ 0 & 0 & \dfrac{-1}{\sqrt{6}} \end{bmatrix} \end{aligned} \tag{25}$$

in which $F_{\text{norm}} = \|\boldsymbol{F}_{\text{in}}\| = \sqrt{3/2}|F_{\text{v}}|$ is the Euclidean norm of the fabric tensor and $\boldsymbol{n}_{\text{F}}$ is the fabric orientation. The input parameter F_{norm} describes the initial magnitude of the fabric tensor. The distribution of a normalised random anisotropic parameter using equation (25) is described in Fig. 6 for various values of F_{norm} and F_{v}.

As shown in Fig. 6, F_{v} and F_{norm} control the distribution of the contact normal related anisotropic features. The sign of F_{v} determines the major principal fabric direction and its

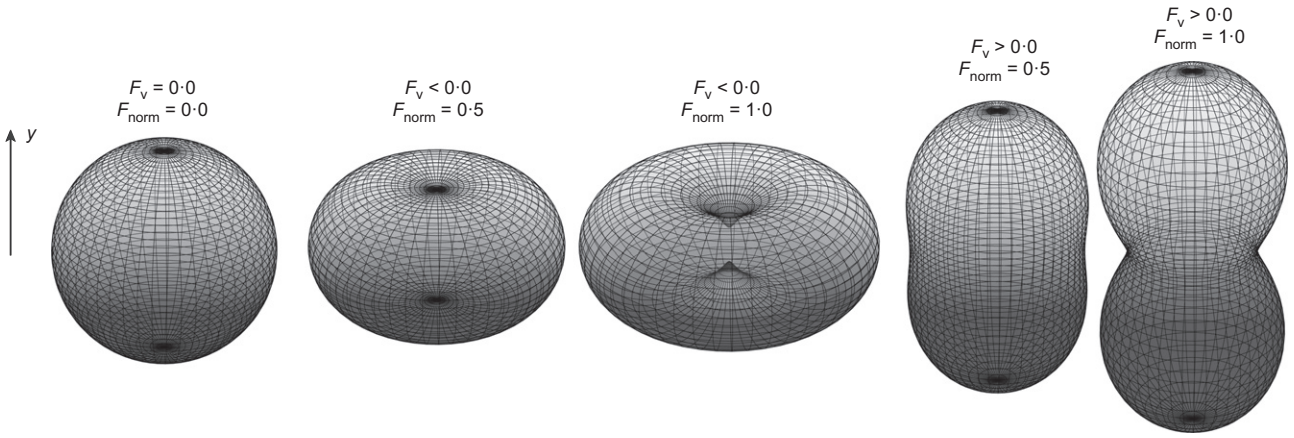

Fig. 6. Spatial distribution of an arbitrary anisotropic parameter for different values of F_{norm} and F_v

magnitude, which can be related to F_{norm} through $F_{norm} = \sqrt{3/2}|F_v|$, determines the ratio of the magnitude of the fabric tensor in the major and minor directions. For the scenario described in equation (24), $F_v > 0$ and $F_v < 0$ yield a fabric structure where the contact normals are concentrated in the vertical (i.e. y-axis) and horizontal directions, respectively, and an increase in F_{norm} distorts the fabric tensor by stretching it in its major principal direction while compressing it in its minor direction. Generally, during the depositional process of soil, the long axis of particles tends to be oriented perpendicularly to the deposition direction, which results in all contact normals being concentrated in the deposition direction (Sun *et al.*, 2019). Hence, F_v in equation (24) mostly takes values greater than 0. From the numerical point of view, unlike e_A, F_{norm} provides a control over the level of downward scaling of the DSL over different directions, such that in the case where the deviator loading aligns with the major fabric direction a positive value of A^i_{fab} results in less downward movement; compare with the case where the deviator loading aligns with the minor fabric direction, in which a negative value of A^i_{fab} is obtained. It is important to mention that, if there is a change in the deposition direction – that is if the deposition direction deviates from the y-direction, the corresponding fabric tensor can be obtained by an orthogonal transformation.

In classical ACST-based models, the deviatoric fabric tensor described in equation (25) is directly employed together with the unit loading direction, which is another tensorial quantity, to calculate the fabric anisotropic variable, $A_{fab} = \boldsymbol{F}:\boldsymbol{n}$. The scalar quantity A_{fab} is then involved in relevant constitutive formulations. In this work, an alternative method has been proposed within the multilaminate framework. The tensorial quantities, namely the deviatoric fabric tensor and loading direction, have been downscaled to their vectorial counterparts – that is to local fabric vectors (or fabric traction vectors) and local unit loading directions, respectively. Even though the local loading direction in its vector form is readily available in equation (27), a definition for the initial fabric vector is needed. It has already been mentioned that, in the employed multilaminate framework, sampling planes are positioned such that they approximate a sphere and the distribution of sampling planes and their normals do not have a directional bias. This feature enables the framework to approximate an isotropic tensor by downscaling the physical quantity held by the tensor into a set of vectors in the normal directions to the planes. However, in order to downscale a tensor with a non-zero deviatoric component, it is necessary to calculate another set of vectors deviating from their isotropic measures (i.e. the sampling planes normal directions) to approximate the non-zero deviatoric part of the tensor. In this paper, the deviation of the vectorial physical quantities from their isotropic direction at each sampling plane is calculated using fabric vectors which are defined as $\boldsymbol{F}^i_{in} = \boldsymbol{F}_{in}\boldsymbol{n}_i$.

Following the description of the fabric tensor and its vectorial counterparts at the sampling planes, the local fabric anisotropic variable (FAV) is calculated as

$$A^i_{fab} = \boldsymbol{F}^i \mathbf{n}^{dev}_i = F^i_{norm}\left(\mathbf{n}^i_F \mathbf{n}^{dev}_i\right) \tag{26}$$

where $\mathbf{n}^i_F \mathbf{n}^{dev}_i$ represents the scalar measure of the relative orientation between the local fabric vector $\boldsymbol{F}^i$ and the local unit deviator stress vector $\mathbf{n}^{dev}_i$. The local unit deviator stress vector $\mathbf{n}^{dev}_i$ is derived from the global deviator stress tensor $\boldsymbol{\sigma}^*$ as

$$\mathbf{n}^{dev}_i = \frac{\boldsymbol{\sigma}^* \boldsymbol{n}_i}{|\boldsymbol{\sigma}^* \boldsymbol{n}_i|} \tag{27}$$

Prior to shearing, the initial fabric vector at a specific plane i is calculated as a traction vector of the initial global fabric tensor – that is $\boldsymbol{F}^i_{in} = \boldsymbol{F}_{in}\boldsymbol{n}_i$, and upon shearing it starts to evolve to a particular fabric vector $\boldsymbol{F}^i$ depending on the accumulated plastic shear strain at the relevant plane, equation (31). At the critical state, the local fabric direction vector $\mathbf{n}^i_F$ becomes coaxial with the local loading direction $\mathbf{n}^{dev}_i$ and the local fabric vector reaches its critical state value $\boldsymbol{F}^i_c$ – that is $\boldsymbol{F}_{in} \rightarrow \boldsymbol{F}^i_{in} \rightarrow \boldsymbol{F}^i \rightarrow \boldsymbol{F}^i_c$. In this model, different from the current ACST applications, instead of considering the global loading direction and a global definition of the fabric tensor, the local loading direction $\mathbf{n}^{dev}_i$, which evolves uniquely at each sampling plane depending on the applied load, has been used. It is important to note that, in this model, the fabric vector throughout the deformation process is normalised by its critical value – that is, by local deviator stress – and, for the sake of simplicity, the critical fabric is set equal to the loading direction – that is, $\boldsymbol{F}^i_c = \mathbf{n}^{dev}_i$.

To sum up, at the critical state the premises set out by ACST are achieved as

$$\boldsymbol{F}^i \rightarrow \boldsymbol{F}^i_c = \mathbf{n}^{dev}_i \text{ and}$$
$$A^i_{fab} = \left|\mathbf{n}^{dev}_i\right|\left(\mathbf{n}^{dev}_i \mathbf{n}^{dev}_i\right) = 1{\cdot}0$$

Fabric evolution

The initial microstructure of the soil changes during the course of loading, and ignoring that change may result in a deviation from both experimental and granular level DEM observations. Most of the available evolution formulations are derived as a function of changing stress ratio and/or

plastic strain rate. Experimental studies by Oda *et al.* (1985), Oda *et al.* (1982) and Oda & Konishi (1974) revealed the link between contact normal evolutions and the applied stress path. Based on these observations, Wan & Guo (2004) proposed a simple evolution rule

$$\dot{\boldsymbol{F}} = k \cdot \dot{\boldsymbol{\eta}} \tag{28}$$

where a linear relationship between the change in stress ratio $\dot{\boldsymbol{\eta}}$ and the fabric tensor was established by using a constant k. Equation (28) yields a constant fabric at the critical state when $\dot{\boldsymbol{\eta}} \to 0$. This linear relationship was upscaled by Hu (2015) with a non-linear counterpart

$$\dot{\boldsymbol{F}} = k_1(1 + k_2\|\boldsymbol{\eta}\|) \cdot \dot{\boldsymbol{\eta}} \tag{29}$$

Another commonly used plastic strain-driven fabric evolution formulation has been proposed by Li & Dafalias (2012)

$$\dot{\boldsymbol{F}} = k(\boldsymbol{F}_{\mathrm{c}} - \boldsymbol{F})\left|\dot{\varepsilon}_q^{\mathrm{p}}\right| \tag{30}$$

where $\boldsymbol{F}_{\mathrm{c}}$ stands for the critical fabric tensor and $\varepsilon_q^{\mathrm{p}}$ is the plastic deviatoric strain.

Equations (28) and (30) both provide an evolution such that the fabric tensor reaches a critical value, $\boldsymbol{F}_{\mathrm{c}}$. However, the evolutions of the stress ratio and plastic strain rates are inversely proportional such that, at the initial stages of shearing, the soil shows limited plastic strains but a rapid increase in stress ratio and the opposite happens towards the critical state. Hence, equations (28) and (30) provide different types of evolution. In addition, it should be noted that the use of equations (28) or (29) in a plasticity theory results in a change in the fabric tensor upon elastic unloading. Furthermore, under complex loading conditions such as SPAR at fixed stress principal values with $\dot{\boldsymbol{\eta}} = 0$, equations (28) and (29) miss out the intense fabric changes observed in laboratory experiments.

The fabric evolution constant k controls the evolution speed of the fabric tensor per stress ratio/plastic strain increment and determines how fast it will reach its critical state value. Hence, an inevitable concern arises about the stress path dependency of the fabric evolution. In this paper, equation (30) with a path-independent evolution constant k has been converted to its vectorial form as $\dot{\boldsymbol{F}}_i = k\left(\boldsymbol{F}_{\mathrm{c}}^i - \boldsymbol{F}_i\right)|\dot{\varepsilon}_\gamma^{\mathrm{p}}|$ and then the implicit time integration of the vectorial fabric evolution formulation is derived as

$$\boldsymbol{F}_i^{t+\Delta t} = \boldsymbol{F}_{\mathrm{c}}^i + \left(\boldsymbol{F}_i^t - \boldsymbol{F}_{\mathrm{c}}^i\right)\mathrm{e}^{-k\Delta\varepsilon_\gamma^{\mathrm{p}}} \tag{31}$$

Note that, in the above fabric evolution formulation, the micro-level plastic shear strain $\varepsilon_\gamma^{\mathrm{p}}$ has been used instead of its global deviatoric counterpart $\varepsilon_q^{\mathrm{p}}$. In contrast to classical continuum models in which a single scalar fabric anisotropic variable defines the anisotropic state of the soil, the proposed formulation yields various fabric scalars – that is, A_{fab}^i values for the different sampling planes – which further enhances the direction- and history-dependent fabric evolution. Even though the speed of reaching $\boldsymbol{F}_{\mathrm{c}}^i$ depends on the local plastic shear strain rate at the corresponding sampling plane, under continuous plastic shearing the fabric vector $\boldsymbol{F}^i$ becomes identical to $\boldsymbol{F}_{\mathrm{c}}^i$ and fulfils the anisotropic critical state theory requirements.

In Fig. 7, each line shows the evolution of A_{fab} at the relevant sampling plane – that is, A_{fab}^i. Even though a single fabric tensor describing the initial fabric is defined using equation (25), equation (26) yields different A_{fab}^i values at different sampling planes due to different $\mathbf{n}_i^{\mathrm{dev}}$ components. Hence, at the beginning of shearing, different A_{fab}^i values are obtained at the different sampling planes. Upon shearing, the locally driven evolution formulation in equation (31) yields different fabric evolutions depending on the local plastic shear strain accumulations, and the subplot in Fig. 7 shows how the speed of the evolution varies at each sampling plane.

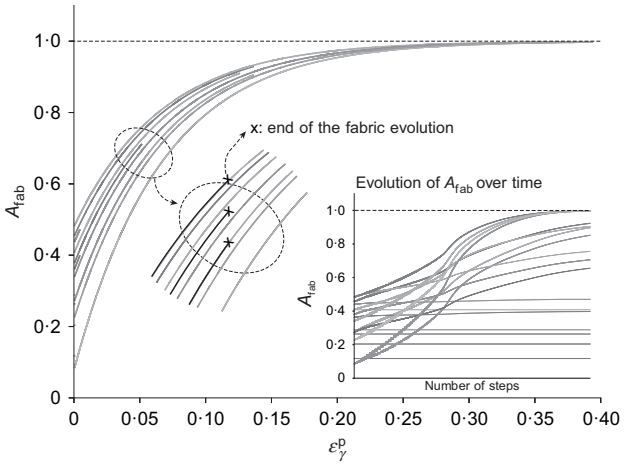

Fig. 7. Evolution of fabric variable A_{fab} with local plastic strain accumulations (and number of steps in subplot) during a triaxial compression test

Finally, it is worth noting that, in the proposed fabric evolution framework, the orientations of the sampling planes which are defined by their unit normals $\boldsymbol{n}_i$ are not changing. In other words, in this paper, sampling planes with their prescribed orientations are used to monitor the fabric changes during shearing rather than keeping track of the contact normals and evolving with them. Even though changing the orientations of the sampling planes together with the changing contact normal distribution – that is changing the spherical shape in Fig. 1 and making it evolve during deformation – sounds attractive, the resultant framework becomes highly unstable. This is because the integration over sampling planes which is carried out to find the global counterpart of the local plastic strains depends on the sampling plane orientations and weight coefficient as shown in equation (4). Such a framework could be attained with an upgraded numerical integration formulation that takes account of the evolving contact normals.

MODEL CALIBRATION AND VALIDATION

Calibration of material parameters

The proposed model requires the calibration of 13 parameters, whose descriptions and values for Toyoura sand used in the current simulations are listed in Table 1. Here, a brief description of the calibration process is given.

The calibration of the elastic part of the model requires resonant column or bender element tests, which are mostly not available. In this paper, the elastic parameters G_{ref} and G_{ratio} for Toyoura sand were calibrated using the resonant column and torsional shear tests from Iwasaki *et al.* (1978). The critical state parameters are all physical parameters: $e_{\mathrm{c},0}$, h_{s} and n are used to define the CSL in void ratio–mean effective stress space, and require tests at large shear strain in which the soil reaches the critical state. The role and calibration of the critical state parameters are similar to those for hypoplasticity and more details can be found in Herle & Gudehus (1999). The constant-volume friction angle φ'_{cv} differs from the Lode angle-dependent critical state friction angle φ'_{cs}. In this model, the material response is formulated using the interparticle friction angle, which is independent of the mode of shearing. For the determination of φ'_{cv}, the φ'_{cs} value in triaxial

Table 1. The constitutive model parameters

Category	Parameter	Toyoura sand	Description
Elasticity	G_{ref}	1400	Reference shear modulus value
	G_{ratio}	3	Small-strain stiffness ratio
	v	0·17	Poisson's ratio
Critical state	$e_{c,0}$	0·934	Critical void ratio at zero pressure
	h_s	20 000 kPa	Hardness parameter
	n	0·74	Exponential stiffness parameter
	φ'_{cv}	31·2°	Constant volume friction angle
Hardening	A_{mat}	0·0055	Plastic stiffness constant
	α	2·3	Exponential constant controlling φ'_{mob}
	β	3	Exponential constant controlling ψ_{mob}
Fabric	F_{norm}	0·515 (dry)/0·41 (wet)	Initial fabric norm
	e_A	0·08 (dry)/0·05 (wet)	Fabric constant for CSL deviation
	k	5·2	Fabric evolution constant

compression can be used – that is, $\varphi'_{cv} = \varphi'_{cs(triax.\ comp)}$. The hardening parameter A_{mat} needs to be calibrated against data from drained triaxial tests by trial and error. The exponential parameters α and β can be back-calculated from peak friction and phase transformation angles through equations (6) and (14), respectively, as shown in Wan & Guo (1999). However, during the back-calculation, instead of the critical void ratio e_c, the dilatancy void ratio e_d should be used as per equation (23), as similarly done in Petalas *et al.* (2020). In this paper, first the set of experimental data provided by Yoshimine *et al.* (1998) and Verdugo & Ishihara (1996) have been used to calibrate the hardening parameters α and β, and then further fine-tuning runs have been carried out to make sure the back-calculated α and β values fit well for the remaining experimental data set. Finally, the calibration of the fabric parameters requires granular level studies, which rarely exist, so that model users will mostly have to determine parameter values through performing trial-and-error calculations. Note that this type of trial-and-error-based fabric tensor calibration requires an extensive data set, including different modes of shearing. However, locating the phase transformation lines using the triaxial compression and extension test results may help to decrease the number of trial runs, since e_A and F_{norm} together locate the DSL in e–p' space.

Validation

In this part of the paper, numerical simulations are compared with experimental test data on Toyoura sand published by various authors. The effect of fabric anisotropy on the stress–strain response of sand is investigated for various monotonic tests including triaxial compression, triaxial extension, simple shear and torsional hollow cylinder tests. The significant effect of the fabric anisotropy upon varying the loading direction with respect to the fabric direction is seen to be properly captured.

Toyoura sand. The set of material parameters used to perform the following simulations is listed in Table 1. It should be noted that, even though all the following figures are for Toyoura sand, different sample preparation methods, namely wet tamping and dry deposited, were used to prepare the specimens and these yielded different initial anisotropic structures. Investigation of the effect of sample preparation methods on the soil fabric is beyond the scope of this paper, but the comparison of experimental data shows that specimens prepared using the dry-deposited method have greater variability in response to principal stress rotation, indicating a higher degree of anisotropy. In this paper, in order to capture that difference, a different set of fabric parameters is used for the different sample preparation methods. For the case of Toyoura sand, using two different values of F_{norm}, which controls the initial fabric anisotropy, and two different values of fabric constant e_A provided reasonable estimates; see Table 1. Note that, in the following comparisons, the simulation and experimental results are shown by solid and broken lines, respectively.

Model performance. The first set of simulations is performed for drained triaxial compression tests on wet-tamped Toyoura sand. A total of six experiments carried out by Verdugo & Ishihara (1996), under two different consolidation pressures of 100 kPa and 500 kPa, and various initial void ratios, are compared with simulations in Fig. 8. The volumetric changes are adequately captured, as shown in the figure. An additional set of drained simulations is performed for torsional simple shear (TSS) tests on dry-deposited Toyoura sand. The TSS tests were carried out by Pradhan *et al.* (1988) and relatively more complex loading paths were followed such that the specimens at low confining pressures ($\approx$ 5 kPa) were first anisotropically consolidated (K_0-consolidation) up to an initial axial stress σ_a and then sheared in torsion under constant axial stress. The comparison of the simulations and experimental data is presented in Fig. 9. The proposed model satisfactorily predicts the overall response.

Figure 10 and Figs 11–16 show simulations of the undrained response of wet-tamped and dry-deposited Toyoura sand, respectively, for a wide range of stress states and initial relative densities. As can be seen from these figures, depending on the stress state and relative density which are included in the state-dependent formulations, the simulation results reflect the significant variations in response recorded in the experiments. It should be emphasised that the addition of the stress-dependent term in the stiffness parameter A formulation in equation (8) provides a noticeable contribution to the model's performance over a wide stress range and different stress paths.

In Fig. 11, a series of triaxial compression and extension tests, along with their simulation results, is presented. In these simulations, specimens having a similar initial state and fabric have been sheared in different directions. As a result, while specimens under compression showed dilative behaviour, all the extension tests resulted in flow liquefaction. This drastic change observed in the experimental data has been well captured by the proposed model.

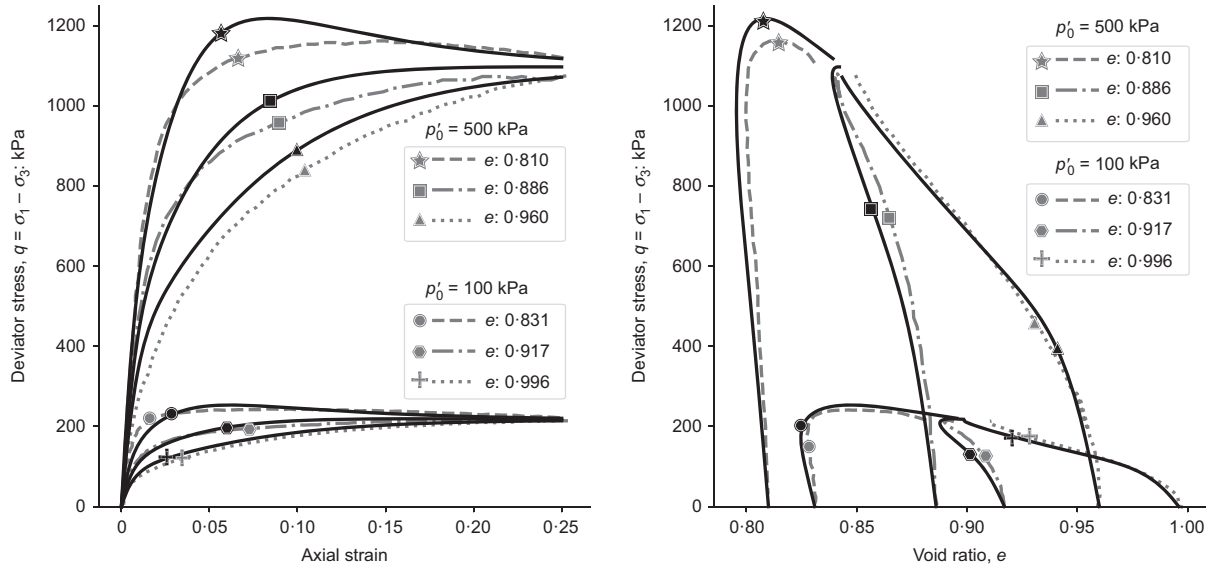

Fig. 8. Simulation of drained triaxial compression tests; data after Verdugo & Ishihara (1996)

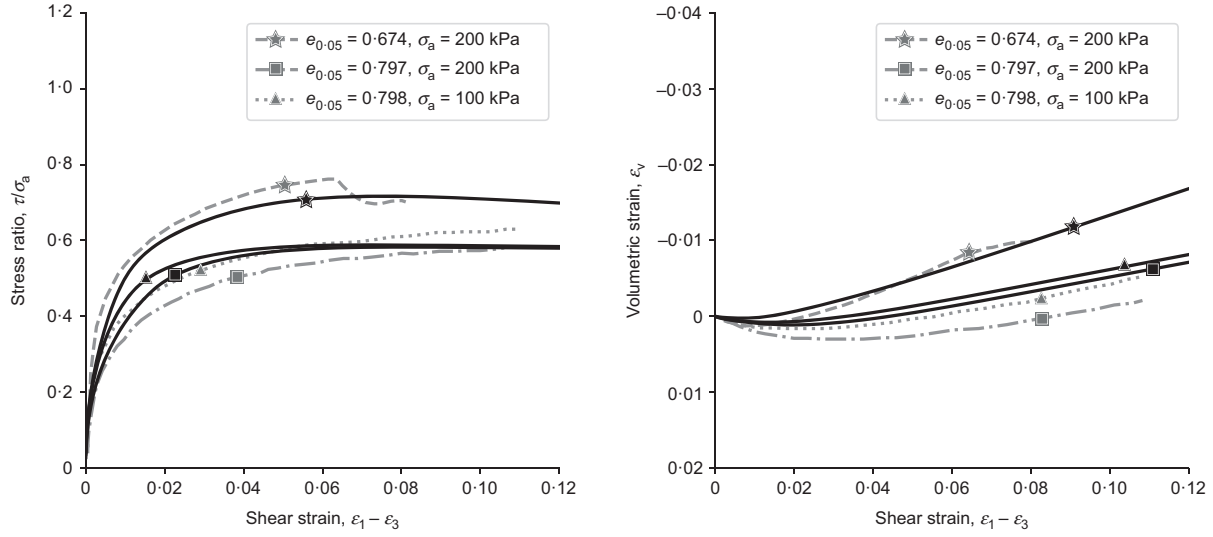

Fig. 9. Drained torsional simple shear tests; data after Pradhan *et al.* (1988)

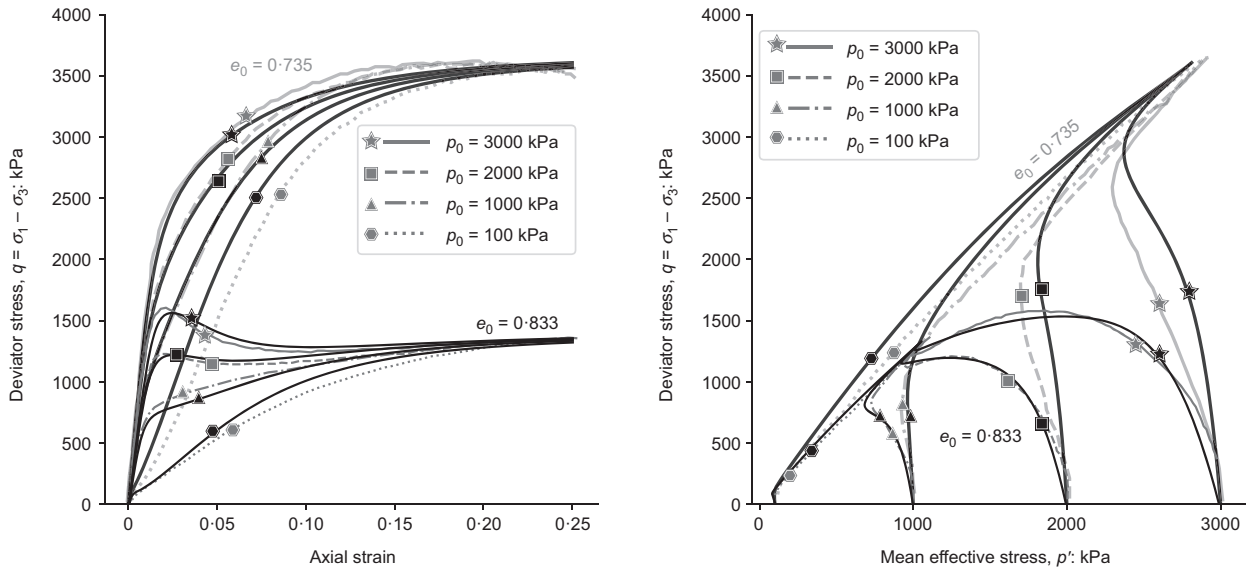

Fig. 10. Undrained triaxial compression tests on dense and medium dense specimens; data after Verdugo & Ishihara (1996)

During a simple shear test, the restricted rotation in the principal stresses greatly influences the material behaviour. Although a full 180° principal stress rotation cannot be achieved, quite substantial principal stress rotations approaching as much as 60° can be observed in simple shear tests, as shown by Gutierrez *et al*. (2009). In Fig. 12, the simulation results show some deviation from the experimental data, although the trends are captured.

So far, the drained and undrained responses of Toyoura sand under various initial states have been compared with simulation results in Figs 8–12. Although these results validate the model's capability to handle different initial states and the effectiveness of the proposed state-dependent formulations in the constitutive model, since all these simulations involve triaxial or simple shear tests in which there is no control over the orientation of principal stresses, the influence of the anisotropy formulation on the simulation performance is difficult to observe. Hence, in the remainder of this paper, in addition to triaxial and simple shear tests, torsional hollow tests will be presented. These results provide a better way to evaluate the effectiveness of the fabric formulation proposed in this model.

In Figs 13–15, stress ratio-controlled hollow cylinder tests are compared with simulation results. In these tests, soil specimens with similar initial states were sheared in different directions as indicated by α_{ani}, which represents the angle between the major principal fabric direction and the major principal stress direction, under constant intermediate principal stress coefficient, $b = (\sigma'_2 - \sigma'_3)/(\sigma'_1 - \sigma'_3)$.

For similar initial densities and stress states, an increase in both b and α_{ani} values in Figs 13–15 results in less dilative/more contractive behaviour, which is well captured

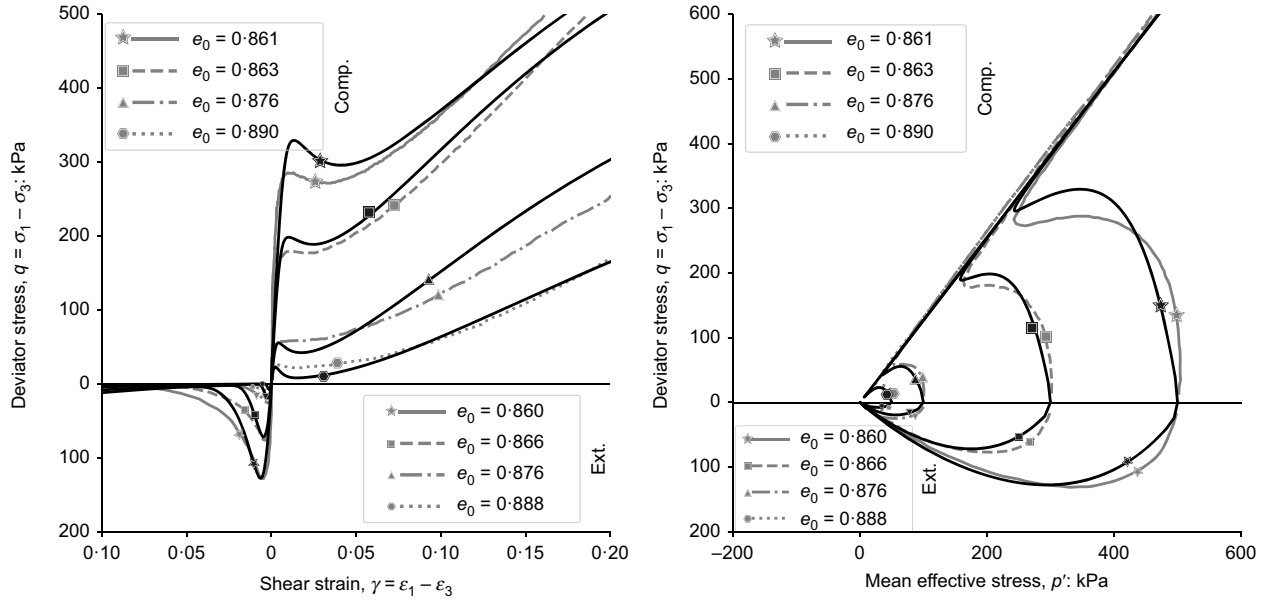

Fig. 11. Undrained triaxial compression and extension tests; data after Yoshimine *et al*. (1998) (note: 'Comp.', compression; 'Ext.', extension)

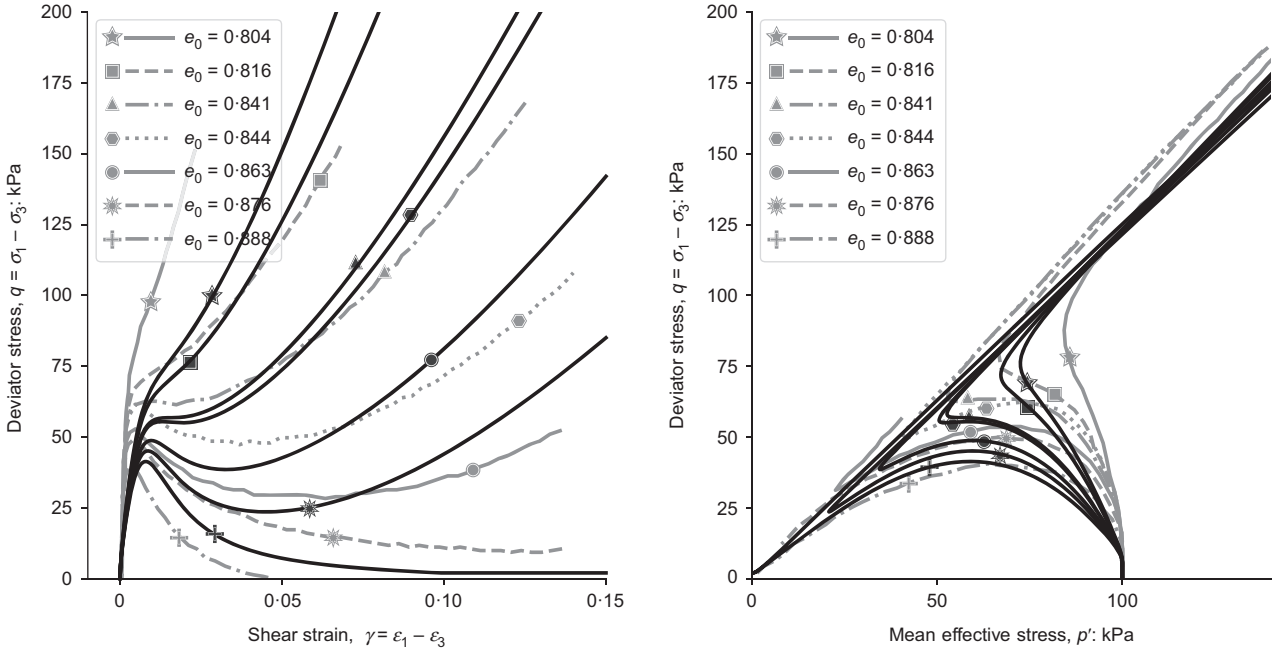

Fig. 12. Undrained simple shear tests; data after Yoshimine *et al*. (1998)

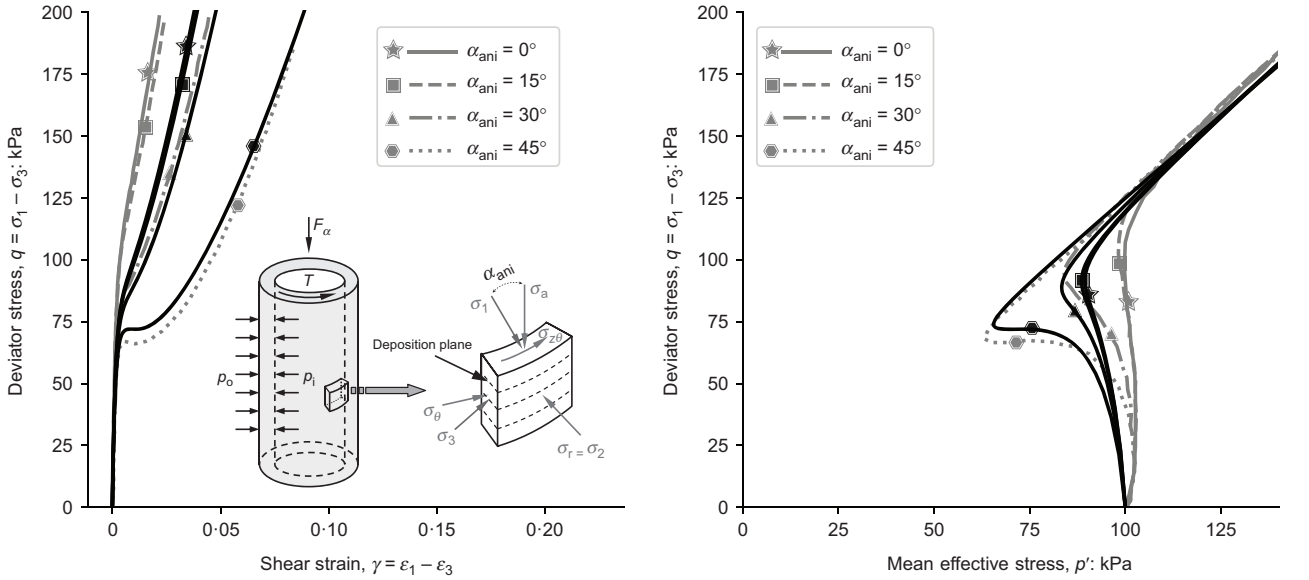

Fig. 13. Torsional hollow cylinder test with principal stress rotation, under constant $b = 0$ and $e_0 = 0{\cdot}82$–$0{\cdot}829$; data after Yoshimine *et al.* (1998)

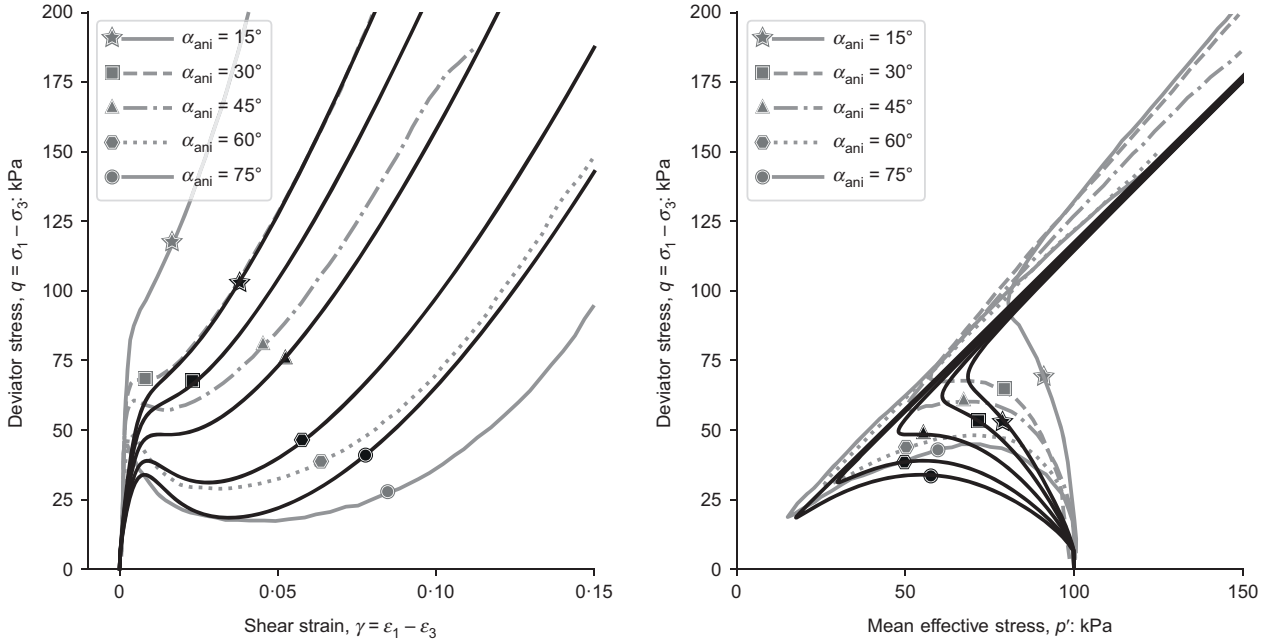

Fig. 14. Torsional hollow cylinder test with principal stress rotation, under constant $b = 0{\cdot}5$ and $e_0 = 0{\cdot}821$–$0{\cdot}828$; data after Yoshimine *et al.* (1998)

by the proposed model. Even though the critical state stress ratios in simulations with $b = 0$ and $b = 1$ match the experimental data in Figs 13 and 15, the multilaminate yield surface given in Fig. 4 underestimates the critical state stress ratio for Toyoura sand for b values between 0 and 1, which can be observed in Figs 14 and 16. Experimental results for Toyoura sand show a better match with the yield surface denoted by Sanisand in Fig. 4.

Finally, the torsional shear tests from Nakata *et al.* (1998) on relatively looser specimens (e.g. $D_R = 30\%$) are shown in Fig. 16. In this figure, the deviatoric stress and the deviatoric strain are calculated as $q_N = \sqrt{0{\cdot}5\left[(\sigma_1' - \sigma_2')^2 + (\sigma_2' - \sigma_3')^2 + (\sigma_3' - \sigma_1')^2\right]}$ and $\gamma_N = \sqrt{2\left[(\varepsilon_1 - \varepsilon_2)^2 + (\varepsilon_2 - \varepsilon_3)^2 + (\varepsilon_3 - \varepsilon_1)^2\right]/9}$, respectively. These results show the effectiveness of both the state dependency and fabric formulations in the proposed model to capture the experimental data. Based on these observations it may be concluded that, for a given stress path, the soil shows less dilative/more contractive behaviour as the angle between the major principal stress and fabric directions increases. These loading and fabric orientation-dependent behaviours are well captured with the proposed model.

CONCLUSIONS

In this paper, a state-dependent constitutive model within the multilaminate framework has been proposed for anisotropic sands. The potential capability of the multilaminate framework to handle the effect of principal stress rotation

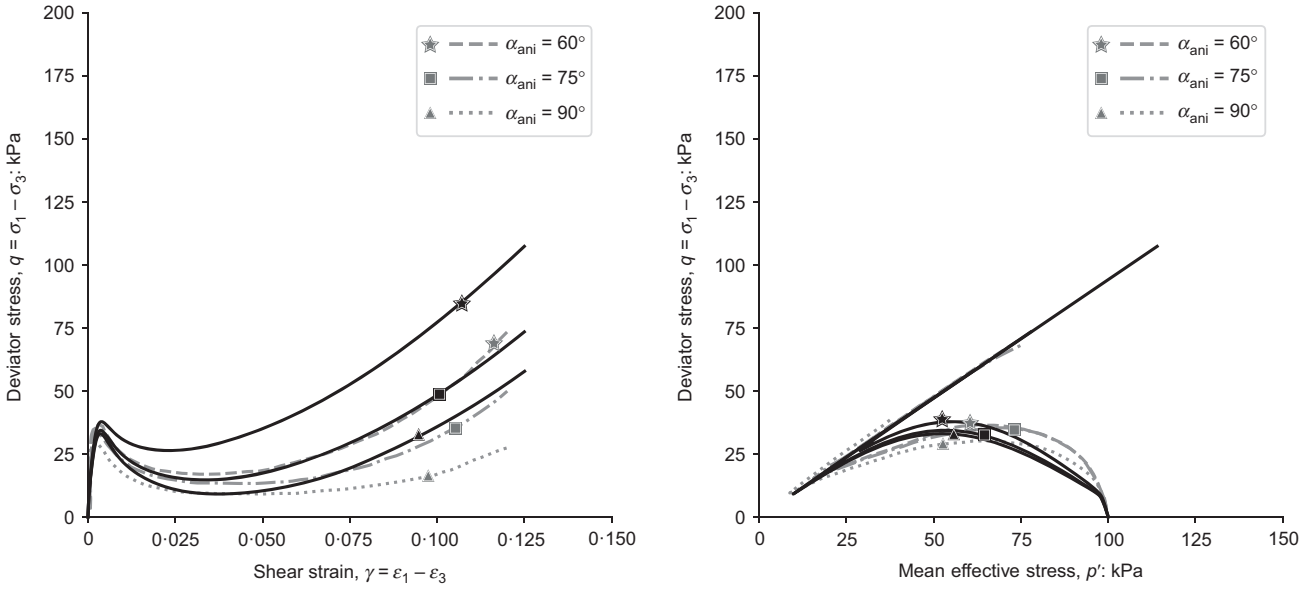

Fig. 15. Torsional hollow cylinder test with principal stress rotation, under constant $b = 1{\cdot}0$ and $e_0 = 0{\cdot}825 - 0{\cdot}826$; data after Yoshimine *et al.* (1998)

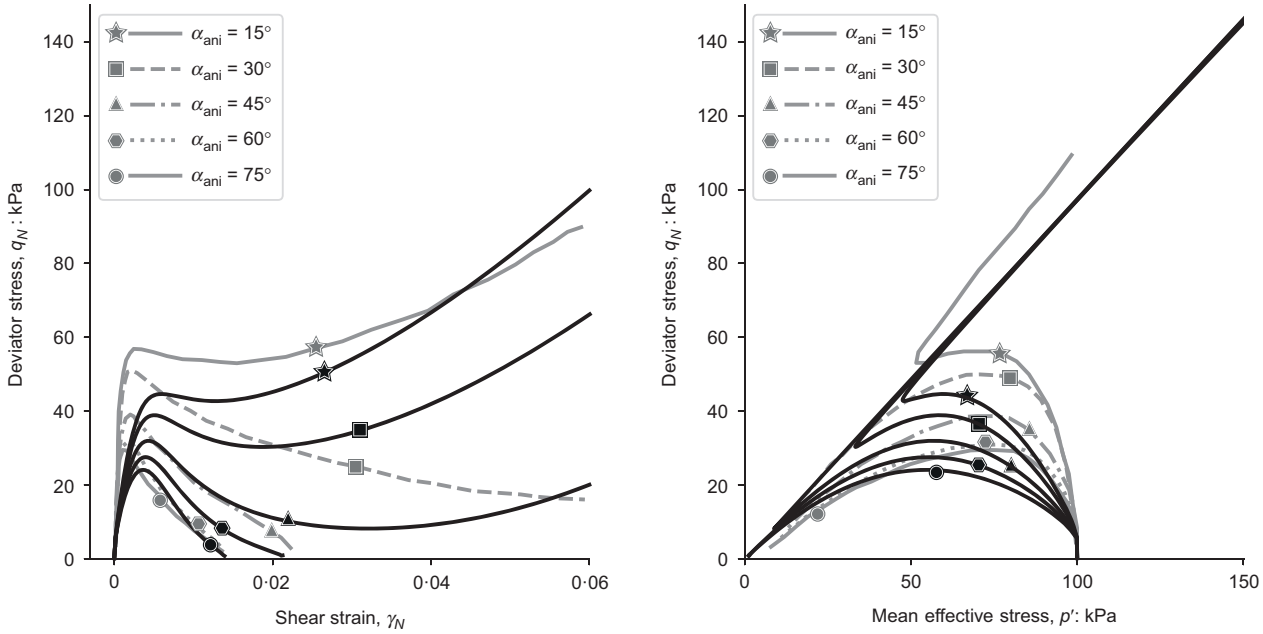

Fig. 16. Torsional hollow cylinder tests on loose specimens ($D_R = 30\%$), under constant $b = 0{\cdot}5$; data after Nakata *et al.* (1998)

and induced anisotropy has been further enhanced by incorporating ACST. Fabric effects have been introduced into the model through the use of a locally evolving fabric vector $\boldsymbol{F}^i$ and then converted to evolving scalar constitutive ingredients which vary over the sampling planes. In this model, instead of stress/strain invariants, using normal and shear components at local sampling planes provides a more intuitively understandable constitutive formulation. Similarly, using sampling planes distributed in 3D stress space provides a rather physical and direction-dependent meaning for the tensorial fabric formulation. Finally, the undrained performance of the model at low mobilised friction angles was improved by suppressing plastic strain accumulation inside the small-strain zone.

The performance of the proposed model has been verified through the simulation of laboratory data for Toyoura sand. The influence of different initial states, different initial fabrics arising from different sample preparation methods, principal stress rotation and various stress paths (e.g. fixed intermediate principal stress ratios and restricted rotation of principal stresses observed in simple shear tests) have been satisfactorily simulated with a single set of material parameters, only varying the fabric parameters. The use of a single set of fabric parameters may result in less accurate predictions in the case when different sample preparation methods are involved. The comparisons between model response and published experimental data show that the proposed constitutive framework is well able to simulate the anisotropic behaviour of sands.

ACKNOWLEDGEMENT

This work is part of the research programme DeepNL/SOFTTOP with project number DEEP.NL.2018.006,

financed by the Netherlands Organisation for Scientific Research (NWO).

NOTATION

A	plastic stiffness parameter
A_{fab}^{i}	fabric anisotropic variable (FAV)
$A_{\text{mat},i}$	minimum value of the plastic stiffness parameter
b	intermediate principal stress coefficient
D_R	relative density
e	void ratio
e_0	initial void ratio
$e_{0{\cdot}05}$	void ratio at 0·05 kgf/cm^2 (≈5 kPa)
e_A	fabric constant, determines the deviation of the dilatancy state line (DSL) from the critical state line (CSL)
e_{c}	critical state void ratio
$e_{\text{c},0}$	critical state void ratio at zero stress
e_{d}	dilatancy void ratio (anisotropic measure of e_{c})
$\boldsymbol{F}$	fabric tensor
F_{h}	principal fabric component in horizontal direction
$\boldsymbol{F}_{\text{in}}$	initial fabric tensor
$\boldsymbol{F}^{i}$	a particular fabric vector of the ith sampling plane
$\boldsymbol{F}_{\text{c}}^{i}$	critical state value of fabric vector of the ith sampling plane
$\boldsymbol{F}_{\text{in}}^{i}$	initial fabric vector of the ith sampling plane
F_{v}	principal fabric component in vertical direction
f	local yield function
G_0	maximum (elastic) shear modulus
G_{ref}	reference shear modulus
G_{small}	small-strain shear modulus
g_i	plastic potential of the ith sampling plane
h_{s}	critical state line model constant
$\boldsymbol{I}$	second-order identity tensor
k	fabric evolution constant
M_{c}	critical state stress ratio in triaxial compression test
M_{e}	critical state stress ratio in triaxial extension test
m	$1 - n$
n	critical state line model constant
$\boldsymbol{n}_{\text{F}}$	fabric orientation
$\mathbf{n}_{\text{F}}^{i}$	unit fabric direction vector of the ith sampling plane
$\boldsymbol{n}_i$	unit normal (or direction cosine) vector of the ith sampling plane
$\mathbf{n}_i^{\text{dev}}$	unit deviator loading vector of the ith sampling plane
p'	mean effective stress
p_{at}	atmospheric pressure
$\mathbf{T}_i$	transformation matrix of the ith sampling plane
w_i	weight coefficient of the ith sampling plane
α	exponential model parameter controlling bounding state line
β	exponential model parameter controlling dilatancy state line
γ_{small}	threshold shear strain for small-strain range
$\boldsymbol{\varepsilon}_i^{\text{p}}$	plastic strain vector at the ith sampling plane
η	stress ratio
λ_i	plastic multiplier of the ith sampling plane
$\boldsymbol{\sigma}'$	Cauchy stress tensor
$\boldsymbol{\sigma}^{*}$	deviatoric stress tensor
σ'_{dev}	magnitude of deviator stress component of a traction stress vector
$\boldsymbol{\sigma}'_i$	traction stress vector at the ith sampling plane
σ'_{n}	magnitude of normal component of a traction stress vector
τ	magnitude of shear stress component of a traction stress vector
ϕ_{kj}	statistical distribution of contact normals
φ'_{cs}	critical state friction angle (global)
φ'_{cv}	constant volume friction angle (local)
φ'_{mc}	maximum contraction friction angle (local)
φ'_{mob}	mobilised friction angle (local)
φ'_{peak}	peak friction angle (local)
ψ	state parameter

REFERENCES

Argyris, J. H., Faust, G., Szimmat, J., Warnke, E. P. & Willam, K. J. (1974). Recent developments in the finite element analysis of prestressed concrete reactor vessels. *Nucl. Engng Des.* **28**, No. 1, 42–75.

Azami, A., Pietruszczak, S. & Guo, P. (2010). Bearing capacity of shallow foundations in transversely isotropic granular media. *Int. J. Numer. Analyt. Methods Geomech.* **34**, No. 8, 771–793.

Bažant, Z. P. & Caner, F. C. (2005). Microplane model M5 with kinematic and static constraints for concrete fracture and anelasticity. I: theory. *J. Engng Mech.* **131**, No. 1, 31–40.

Bažant, P. & Oh, B. (1986). Efficient numerical integration on the surface of a sphere. *ZAMM – J. Appl. Math. Mech./Z. Angew. Math. Mech.* **66**, No. 1, 37–49.

Been, K. & Jefferies, M. G. (1985). A state parameter for sands. *Géotechnique* **35**, No. 2, 99–112, https://doi.org/10.1680/geot.1985.35.2.99.

Benz, T. (2007). *Small-strain stiffness of soils and its numerical consequences.* PhD thesis, University of Stuttgart, Stuttgart, Germany.

Carol, I. & Bazant, Z. P. (1997). Damage and plasticity in microplane theory. *Int. J. Solids Structs* **34**, No. 29, 3807–3835.

Chang, K. T. & Sture, S. (2006). Microplane modeling of sand behavior under non-proportional loading. *Comput. Geotech.* **33**, No. 3, 177–187.

Cubrinovski, M. & Ishihara, K. (1998). Modelling of sand behaviour based on state concept. *Soils Found.* **38**, No. 3, 115–127.

Dafalias, Y. & Manzari, M. (2004). Simple plasticity sand model accounting for fabric change effects. *J. Engng Mech.* **130**, No. 6, 622–634.

Dafalias, Y. F., Papadimitriou, A. G. & Li, X. S. (2004). Sand plasticity model accounting for inherent fabric anisotropy. *J. Engng Mech.* **130**, No. 11, 1319–1333.

Dashti, H., Sadrnejad, S. A. & Ganjian, N. (2019). A novel semi-micro multilaminate elasto-plastic model for the liquefaction of sand. *Soil Dyn. Earthq. Engng* **124**, 121–135.

Duncan, J. M. & Chang, C. Y. (1970). Nonlinear analysis of stress and strain in soils. *J. Soil Mech. Found. Div.* **96**, No. 5, 1629–1653.

Ehret, A., Itskov, M. & Schmid, H. (2010). Numerical integration on the sphere and its effect on the material symmetry of constitutive equations—a comparative study. *Int. J. Numer. Methods Engng* **81**, No. 2, 189–206.

Fang, H. L. (2003). A state-dependent multi-mechanism model for sands. *Géotechnique* **53**, No. 4, 407–420, https://doi.org/10.1680/geot.2003.53.4.407.

Fliege, J. & Maier, U. (1996). *A two-stage approach for computing cubature formulae for the sphere.* Dortmund, Germany: Fachbereich Mathematik, University of Dortmund.

Fu, P. & Dafalias, Y. F. (2011). Fabric evolution within shear bands of granular materials and its relation to critical state theory. *Int. J. Numer. Analyt. Methods Geomech.* **35**, No. 18, 1918–1948.

Fu, P. & Dafalias, Y. F. (2015). Relationship between void- and contact normal-based fabric tensors for 2D idealized granular materials. *Int. J. Solids Structs* **63**, 68–81.

Galavi, V. (2007). *A multilaminate model for structured clay incorporating inherent anisotropy and strain softening*. PhD thesis, Technische Universität Graz (Graz University of Technology), Graz, Austria.

Galavi, V. (2021). Deltasand: a state-dependent double hardening elasto-plastic model for sand: formulation and validation. *Comput. Geotech.* **129**, 103844.

Galavi, V. & Schweiger, H. F. (2010). Nonlocal multilaminate model for strain softening analysis. *Int. J. Geomech.* **10**, No. 1, 30–44.

Guo, N. & Zhao, J. (2013). The signature of shear-induced anisotropy in granular media. *Comput. Geotech.* **47**, 1–15.

Gutierrez, M., Wang, J. & Yoshimine, M. (2009). Modeling of the simple shear deformation of sand: effects of principal stress rotation. *Acta Geotech.* **4**, No. 3, 193–201.

Herle, I. & Gudehus, G. (1999). Determination of parameters of a hypoplastic constitutive model from properties of grain assemblies. *Mech. Cohes.-Frict. Mater.* **4**, No. 5, 461–486.

Hu, N. (2015). *On fabric tensor-based constitutive modelling of granular materials: theory and numerical implementation*. PhD thesis, University of Nottingham, Nottingham, UK.

Iwasaki, T., Tatsuoka, F. & Takagi, Y. (1978). Shear moduli of sands under cyclic torsional shear loading. *Soils Found.* **18**, No. 1, 39–56.

Kruyt, N. P. (2012). Micromechanical study of fabric evolution in quasi-static deformation of granular materials. *Mech. Mater.* **44**, 120–129.

Li, X. S. & Dafalias, Y. F. (2000). Dilatancy for cohesionless soils. *Géotechnique* **50**, No. 4, 449–460, https://doi.org/10.1680/geot.2000.50.4.449.

Li, X. S. & Dafalias, Y. F. (2002). Constitutive modeling of inherently anisotropic sand behavior. *J. Geotech. Geoenviron. Engng* **128**, No. 10, 868–880.

Li, X. S. & Dafalias, Y. F. (2004). A constitutive framework for anisotropic sand including non-proportional loading. *Géotechnique* **54**, No. 1, 41–55, https://doi.org/10.1680/geot.2004.54.1.41.

Li, X. S. & Dafalias, Y. F. (2012). Anisotropic critical state theory: role of fabric. *J. Engng Mech.* **138**, No. 3, 263–275.

Li, X. & Li, X. S. (2009). Micro-macro quantification of the internal structure of granular materials. *J. Engng Mech.* **135**, No. 7, 641–656.

Manzari, M. T. & Dafalias, Y. F. (1997). A critical state two-surface plasticity model for sands. *Géotechnique* **47**, No. 2, 255–272, https://doi.org/10.1680/geot.1997.47.2.255.

Nakata, Y., Hyodo, M., Murata, H. & Yasufuku, N. (1998). Flow deformation of sands subjected to principal stress rotation. *Soils Found.* **38**, No. 2, 115–128.

Niemunis, A. (2003). Anisotropic effects in hypoplasticity. In *Deformation characteristics of geomaterials, recent investigations and prospects* (eds H. DiBenedetto, T. Doanh, H. Geoffroy and C. Sauzéat), pp. 1211–1217. Leiden, the Netherlands: Balkema.

Norouzi, N. & Lashkari, A. (2021). An anisotropic critical state plasticity model with stress ratio-dependent fabric tensor. *Iranian J. Sci. Technol., Trans. Civ. Engng* **45**, No. 4, 2577–2594.

Oda, M. & Koishikawa, I. (1979). Effect of strength anisotropy on bearing capacity of shallow footing in a dense sand. *Soils Found.* **19**, No. 3, 15–28.

Oda, M. & Konishi, J. (1974). Rotation of principal stresses in granular material during simple shear. *Soils Found.* **14**, No. 4, 39–53.

Oda, M., Konishi, J. & Nemat-Nasser, S. (1982). Experimental micromechanical evaluation of strength of granular materials: effects of particle rolling. *Mech. Mater.* **1**, No. 4, 269–283.

Oda, M., Nemat-Nasser, S. & Konishi, J. (1985). Stress-induced anisotropy in granular masses. *Soils Found.* **25**, No. 3, 85–97.

Oztoprak, S. & Bolton, M. D. (2013). Stiffness of sands through a laboratory test database. *Géotechnique* **63**, No. 1, 54–70, https://doi.org/10.1680/geot.10.P.078.

Pande, G. N. & Sharma, K. G. (1983). Multi-laminate model of clays—a numerical evaluation of the influence of rotation of the principal stress axes. *Int. J. Numer. Analyt. Methods Geomech.* **7**, No. 4, 397–418.

Papadimitriou, A. G., Chaloulos, Y. K. & Dafalias, Y. F. (2019). A fabric-based sand plasticity model with reversal surfaces within anisotropic critical state theory. *Acta Geotech.* **14**, No. 2, 253–277.

Petalas, A. L., Dafalias, Y. F. & Papadimitriou, A. G. (2020). Sanisand-F: sand constitutive model with evolving fabric anisotropy. *Int. J. Solids Structs* **188–189**, 12–31.

Pietruszczak, S. & Mroz, Z. (2000). Formulation of anisotropic failure criteria incorporating a microstructure tensor. *Comput. Geotech.* **26**, No. 2, 105–112.

Pietruszczak, S. & Niu, X. (1992). Numerical evaluation of bearing capacity of a foundation in strain softening soil. *Comput. Geotech.* **13**, No. 3, 187–198.

Pradhan, T. B. S., Tatsuoka, F. & Horii, N. (1988). Strength and deformation, characteristics of sand in torsional simple shear. *Soils Found.* **28**, No. 3, 131–148.

Prat, P. C. & Bažant, Z. P. (1991). Microplane model for triaxial deformation of saturated cohesive soils. *J. Geotech. Engng* **117**, No. 6, 891–912.

Qin, J., Zeng, X. & Ming, H. (2016). Centrifuge modeling and the influence of fabric anisotropy on seismic response of foundations. *J. Geotech. Geoenviron. Engng* **142**, No. 3, 04015082.

Richart, F. E., Hall, J. R. & Woods, R. D. (1970). *Vibrations of soils and foundations.* Englewood Cliffs, NJ, USA: Prentice-Hall.

Rowe, P. W. (1962). The stress-dilatancy relation for static equilibrium of an assembly of particles in contact. *Proc. R. Soc. London Ser. A. Math. Phys. Sci.* **269**, No. 1339, 500–527.

Sadrnejad, S. A. & Shakeri, S. (2017). Fabric assessment of damaged anisotropic geo-materials using the multi-laminate model. *Int. J. Rock Mech. Min. Sci.* **91**, 90–103.

Salvatore, E., Modoni, G., Andò, E., Albano, M. & Viggiani, G. (2017). Determination of the critical state of granular materials with triaxial tests. *Soils Found.* **57**, No. 5, 733–744.

Sánchez, F., Prat, P., Galavi, V. & Schweiger, H. (2008). Multilaminate and microplane models: same principles and different solutions for constitutive behaviour of geomaterials. *12th international conference of the International Association for Computer Methods and Advances in Geomechanics*, Goa, India, vol. 2, pp. 911–919.

Santos, J. & Correia, A. (2001). Reference threshold shear strain of soil. Its application to obtain an unique strain-dependent shear modulus curve for soil. *15th international conference on soil mechanics and foundation engineering*, Istanbul, Turkey, pp. 267–270.

Satake, M. (1978). Constitution of mechanics of granular materials through the graph theory. In *Proceedings of the U.S.-Japan seminar on continuum-mechanical and statistical approaches in the mechanics of granular materials* (eds S. C. Cowin and M. Satake), pp. 47–62. Tokyo, Japan: Association for Science Documents Information.

Schanz, T. (1998). *Zur modellierung des mechanischen verhaltens von reibungsmaterialien*. Habilitation thesis, University of Stuttgart, Stuttgart, Germany (in German).

Schanz, T., Vermeer, P. A. & Bonnier, P. G. (1999). The hardening soil model: formulation and verification. In *Beyond 2000 in computational geotechnics* (ed. R. J. Brinkgreve), pp. 281–296. Rotterdam, the Netherlands: Balkema.

Schweiger, H. F., Wiltafsky, C., Scharinger, F. & Galavi, V. (2009). A multilaminate framework for modelling induced and inherent anisotropy of soils. *Géotechnique* **59**, No. 2, 87–101, https://doi.org/10.1680/geot.2008.3770.

Sivathayalan, S. & Vaid, Y. P. (2002). Influence of generalized initial state and principal stress rotation on the undrained response of sands. *Can. Geotech. J.* **39**, No. 1, 63–76.

Søreide, O. K. (2003). *Mixed hardening models for frictional soils.* Dr Ing PhD thesis, Norwegian University of Science and Technology, Trondheim, Norway.

Stroud, A. H. (1971). *Approximate calculation of multiple integrals.* Englewood Cliffs, NJ, USA: Prentice-Hall.

Sun, Q., Zheng, J., He, H. & Li, Z. (2019). Characterizing fabric anisotropy of air-pluviated sands. In *7th International symposium on deformation characteristics of geomaterials (IS-Glasgow 2019)* (eds A. Tarantino and E. Ibraim), E3S Web of Conferences volume 92, article 01003. Les Ulis, France: EDP Sciences.

Tatsuoka, F., Siddiquee, M. S. A., Park, C., Sakamoto, M. & Abe, F. (1993). Modeling stress–strain relations of sand. *Soils Found.* **33**, No. 2, 60–81.

Tsegaye, A. B., Nordal, S. & Benz, T. (2013). On shear-volume coupling in deformation of soils. In *Constitutive modeling of geomaterials – advances and new applications* (eds Q. Yang, J.-M. Zhang, H. Zheng and Y. Yao), pp. 491–500. Berlin/Heidelberg, Germany: Springer.

Uthayakumar, M. & Vaid, Y. P. (1998). Static liquefaction of sands under multiaxial loading. *Can. Geotech. J.* **35**, No. 2, 273–283.

Verdugo, R. & Ishihara, K. (1996). The steady state of sandy soils. *Soils Found.* **36**, No. 2, 81–91.

Vermeer, P. A. & De Borst, R. (1984). Non-associated plasticity for soils, concrete and rock. *HERON* **29**, No. 3, 1–64.

Wan, R. G. & Guo, P. J. (1998). A simple constitutive model for granular soils: modified stress-dilatancy approach. *Comput. Geotech.* **22**, No. 2, 109–133.

Wan, R. G. & Guo, P. J. (1999). A pressure and density dependent dilatancy model for granular materials. *Soils Found.* **39**, No. 6, 1–11.

Wan, R. & Guo, P. (2001). Effect of microstructure on undrained behaviour of sands. *Can. Geotech. J.* **38**, No. 1, 16–28.

Wan, R. G. & Guo, P. J. (2004). Stress dilatancy and fabric dependencies on sand behavior. *J. Engng Mech.* **130**, No. 6, 635–645.

Wan, R. & Guo, P. (2014). Microstructural formulation of stress dilatancy. *C. R. Mécanique* **342**, No. 3, 198–207.

Wang, R., Fu, P., Zhang, J. M. & Dafalias, Y. F. (2017). Evolution of various fabric tensors for granular media toward the critical state. *J. Engng Mech.* **143**, No. 10, 04017117.

Wegener, D. & Herle, I. (2012). Zur steifigkeit bei kleinen dehnungen im rahmen der hypoplastizität. *Gieotechnik* **35**, No. 4, 229–235 (in German).

Wehnert, M. (2006). *Ein beitrag zur drainierten und undrainierten analyse in der geotechnik*. PhD thesis, University of Stuttgart, Stuttgart, Germany (in German).

Wiebicke, M. (2020). *Experimental analysis of the evolution of fabric in granular soils upon monotonic loading and load reversals.* PhD thesis, Dresden University of Technology, Dresden, Germany.

Wiebicke, M., Andò, E., Viggiani, G. & Herle, I. (2020). Measuring the evolution of contact fabric in shear bands with X-ray tomography. *Acta Geotech.* **15**, No. 1, 79–93.

Woo, S. I. & Salgado, R. (2015). Bounding surface modeling of sand with consideration of fabric and its evolution during monotonic shearing. *Int. J. Solids Structs* **63**, 277–288.

Wood, D. M., Belkheir, K. & Liu, M. (1994). Strain softening and state parameter for sand modelling. *Géotechnique* **44**, No. 2, 335–339, https://doi.org/10.1680/geot.1994.44.2.335.

Yang, Z. X. & Wu, Y. (2017). Critical state for anisotropic granular materials: a discrete element perspective. *Int. J. Geomech.* **17**, No. 2, 04016054.

Yang, Z. X., Li, X. S. & Yang, J. (2008). Quantifying and modelling fabric anisotropy of granular soils. *Géotechnique* **58**, No. 4, 237–248, https://doi.org/10.1680/geot.2008.58.4.237.

Yang, Z., Liao, D. & Xu, T. (2020). A hypoplastic model for granular soils incorporating anisotropic critical state theory. *Int. J. Numer. Analyt. Methods Geomech.* **44**, No. 6, 723–748.

Yao, Y., Tian, Y. & Gao, Z. (2017). Anisotropic UH model for soils based on a simple transformed stress method. *Int. J. Numer. Analyt. Methods Geomech.* **41**, No. 1, 54–78.

Yoshimine, M. & Kataoka, M. (2008). Steady state of sand in triaxial extension test. In *Earthquake hazards and mitigation* (eds R. Ayothiraman and H. Hazarika), pp. 431–438. New Delhi, India: I. K. International.

Yoshimine, M., Ishihara, K. & Vargas, W. (1998). Effects of principal stress direction and intermediate principal stress on undrained shear behavior of sand. *Soils Found.* **38**, No. 3, 179–188.

Zhao, C. F. & Kruyt, N. P. (2020). An evolution law for fabric anisotropy and its application in micromechanical modelling of granular materials. *Int. J. Solids Structs* **196–197**, 53–66.

Zhao, C. F., Pinzón, G., Wiebicke, M., Andò, E., Kruyt, N. P. & Viggiani, G. (2021). Evolution of fabric anisotropy of granular soils: X-ray tomography measurements and theoretical modelling. *Comput. Geotech.* **133**, 104046.